Astronomy & Astrophysics manuscript no. output
July 7, 2026

Are the Parker and focused transport equations equivalent for galactic cosmic ray modulation?

J.P. van den Berg[1,2,⋆], N.E. Engelbrecht[1,2], and R.D. Strauss[1,2]

[1] Centre for Space Research, North-West University, Potchefstroom, South Africa
[2] National Institute for Theoretical and Computational Physics (NITheCS), South Africa

Received 10 April 2026

ABSTRACT

Context. The Parker transport equation (TPE) has been the preferred equation for the past 60 years in studies of galactic cosmic ray (GCR) modulation. The focused TPE, however, describes the same processes on a more fundamental level than the Parker TPE by modelling an anisotropic rather than an isotropic distribution. It is usually assumed that the Parker TPE is valid for modelling GCRs, but the two TPEs have not been tested against each other in this context.

Aims. We conducted a first-of-its-kind comparison of these TPEs without particle drifts to test whether they produce the same results under identical diffusion conditions.

Methods. We developed a new model to numerically solve the TPEs for protons under solar-minimum conditions, using stochastic differential equations. The model ensures that the TPEs are as consistent as possible for diffusion by normalising the pitch-angle-dependent diffusion coefficients (DCs) used in the focused TPE to the isotropic DCs used in the Parker TPE.

Results. The Parker TPE overestimates the GCR intensity at Earth's orbit by $\sim 30\%$ at low energies and by $\sim 40\%$ over the poles. This stems from a small first-order anisotropy caused by particle fluxes over the poles. Particles gain easier access to the inner heliosphere by streaming in over the poles, where pitch-angle scattering is generally weaker and the magnetic field is typically less wound. The focused TPE also yields nearly identical results for different pitch-angle dependencies of the DCs.

Conclusions. The description of particle streaming and weak pitch-angle scattering as effective parallel diffusion in the Parker TPE makes it overly diffusive. This suggests that fitting the Parker TPE to observations likely underestimates DCs. Furthermore, GCR spectral and anisotropy data alone cannot distinguish between scattering theories that have similar mean free paths but different pitch-angle dependencies.

Key words. cosmic rays – magnetic fields – solar wind – diffusion – sun: heliosphere – methods: numerical

1. Introduction

High-energy charged particles originating outside the heliosphere, known as galactic cosmic rays (GCRs), diffuse and drift into the heliosphere against the outward-directed solar wind (SW). In general, cosmic rays (CRs) continuously lose energy as they are scattered by turbulence in the heliospheric magnetic field (HMF), a process known as solar modulation. The constant influx of GCRs into the heliosphere, together with long-term solar modulation, allows them to be treated as quasi-stationary. The many scatterings that GCRs experience over the large scales of the heliosphere, together with their entry from all directions, lead to a fairly isotropic and somewhat homogeneous distribution throughout the heliosphere. Since the seminal paper by Parker (1965), the so-called Parker transport equation (TPE; see also Jokipii & Parker 1970; Webb & Gleeson 1979; Moraal 2013) has been widely used for more than 50 years to advance our understanding of CR transport in the isotropic limit (see the reviews by Quenby 1984; Kóta 2013; Engelbrecht et al. 2022a). Numerical modulation codes, which solve this equation to varying degrees of complexity, have yielded results that are sometimes extremely close to spacecraft observations (see e.g. Potgieter 2013; Rankin et al. 2022).

Shortly after Parker's paper, it was realised that a more general TPE is needed for anisotropic distributions. For example, because solar energetic particles (SEPs) propagate preferentially away from the Sun and the HMF focuses them near the Sun, it is necessary to use the so-called focused transport equation (FTE), which includes pitch-angle information (see Roelof 1969; Skilling 1971; Ruffolo 1995). It is widely accepted that the Parker TPE is inadequate for modelling SEPs, even when the focusing effect is taken into account (see e.g. Litvinenko & Noble 2013; Effenberger & Litvinenko 2014; Malkov 2017, 2018; van den Berg et al. 2020). This has led to the use of the so-called telegraph equation and other higher-order approximations of the FTE (see the aforementioned references and those therein). Ultimately, it has become clear that the FTE, with its pitch-angle information, is necessary to model the initial phase of an SEP event while the distribution is isotropising. The very nature of GCRs, however, suggests that their distribution is sufficiently isotropic for the Parker TPE to apply under typical modulation conditions. It has been widely and implicitly assumed that it does, with the only exceptions being anomalous (Isenberg 1997; le Roux et al. 2007) and ultra-high-energy (Maalal & Zhang 2025) CRs, as well as CRs propagating very close to the Sun (Strauss et al. 2022, 2024). However, the Parker TPE would be reliable for GCRs only if it produced intensities identical to those of the FTE under typical modulation conditions.

It follows from deriving the Parker TPE from the FTE, which we discuss in the next section, that any process or situ-

⋆ Corresponding author: 24182869@mynwu.ac.za

Article published by EDP Sciences, to be cited as https://doi.org/10.1051/0004-6361/202660355

ation that renders the distribution insufficiently isotropic makes the Parker TPE an approximation. van den Berg (2023) illustrates this by modelling Jovian electrons under specific hypothetical scenarios. This is noteworthy, as Jovian electrons are a CR species similar to GCRs in that Jupiter is a quasi-stationary source of electrons (Pyle & Simpson 1977; Chenette et al. 1977; Moses 1987) that are usually assumed to be sufficiently isotropic so that the Parker TPE commonly describes their transport (see e.g. Ferreira et al. 2001; Vogt et al. 2020; Strauss et al. 2024; Engelbrecht 2024), but they can potentially deviate from isotropy due to jets (Smith et al. 1976; McKibben et al. 2007; Dunzlaff et al. 2010) and more pronounced spatial gradients. van den Berg (2023) concludes that the Parker TPE is potentially invalid if deterministic pitch-angle changes (such as focusing or mirroring) are not negligible, the parallel mean free path (MFP) is large, perpendicular diffusion is as important as parallel diffusion, there is interplay between pitch-angle scattering and perpendicular diffusion in the previous case, or the pitch-angle diffusion coefficient (PADC) is asymmetric. This not only shows that the Parker TPE may be invalid for Jovian electrons but also identifies the physical mechanisms by which it can fail. Some of these limiting conditions likely hold in the broader heliosphere, particularly those pertaining to diffusion coefficients (i.e. large parallel MFPs, sizeable ratios of the perpendicular to the parallel MFP, and even asymmetric PADCs due to non-zero magnetic or cross helicities[1]).

To the best of our knowledge, the validity of the Parker TPE for studying GCR modulation has not been examined before. This paper aims to highlight how the Parker and focused TPEs could differ using typical, well-tested inputs for transport coefficients and heliospheric plasma parameters in a first-of-its-kind comparison of GCR modulation with both TPEs. The focus of this investigation is to compare the results of the Parker TPE with those of the FTE under identical transport conditions, rather than to reproduce specific GCR observations. We consider and explain the relative differences between solutions of the TPEs, starting by neglecting drifts and focusing only on diffusion. We summarise the theoretical background required for this work in Sect. 2. We describe the numerical model used in the study in Sect. 3, with some of its mathematical details in Appendix A and its validation in Appendix B. We present the results of the comparison in Sect. 4, with some mathematical details in Appendix C. We discuss the results and their implications in Sect. 5, and we summarise this investigation in Sect. 6.

2. Background

A hierarchy of TPEs exists. First, a Fokker-Planck-type equation describes the evolution of the distribution over the entire phase space and is the most complete model; then the FTE for a gyrotropic distribution retains pitch-angle information; finally, a so-called diffusion-advection equation, such as the Parker TPE, describes an isotropic distribution averaged over pitch angle. Assuming that particle gyration about the magnetic field is the fastest process, an average over gyrophase (the angle of gyration about the magnetic field) can be performed to retain pitch-angle information. The pitch angle, α, is the angle between the particle velocity vector and the magnetic field vector, and it indicates the extent to which the particle moves along the field. Usually, the cosine of the pitch angle, $\mu = \cos\alpha$, is employed, where a particle streaming along (only gyrating around) the magnetic field has $\alpha = 0^\circ$ or $\alpha = 180^\circ \implies |\mu| = 1$ ($\alpha = 90^\circ \implies \mu = 0$). If the momentum vectors of the particles are sufficiently scattered by turbulence such that their pitch angles are uniformly distributed, an average over pitch cosine can be performed to neglect pitch-angle information.

The FTE is an evolution equation for the gyrotropic distribution function, $f(\boldsymbol{r}, p, \mu, t)$, of the particle number density per unit momentum volume at position $\boldsymbol{r}$ and time t, with particle momentum p and pitch cosine measured in a non-relativistic flow frame. It is customary to denote quantities measured in the flow frame with a prime, but we omitted the prime in this work for convenience since we did not consider transformations between frames. Similarly, it is customary to denote the distribution function in a mixed frame using a superscript asterisk, but we also omitted this. The equation reads as (Zhang 2006; Zank 2014; Wijsen 2020; van den Berg 2023)

$$\frac{\partial f}{\partial t} + \boldsymbol{\nabla} \cdot (\boldsymbol{v}_{\mathrm{gc}} f) + \frac{1}{p^2}\frac{\partial}{\partial p}\left[p^2 \frac{\mathrm{d}p}{\mathrm{d}t} f\right] + \frac{\partial}{\partial \mu}\left[\frac{\mathrm{d}\mu}{\mathrm{d}t} f\right]$$
$$= \frac{\partial}{\partial \mu}\left[D_{\mu\mu}\frac{\partial f}{\partial \mu}\right] + \boldsymbol{\nabla} \cdot (\mathsf{D}_\perp \cdot \boldsymbol{\nabla} f), \tag{1}$$

where $D_{\mu\mu}(\mu)$ is the PADC and $\mathsf{D}_\perp = D_\perp(\mu)\,(\mathsf{I} - \hat{\boldsymbol{b}}\hat{\boldsymbol{b}})$ is the perpendicular diffusion tensor for axisymmetric turbulence, with $D_\perp(\mu)$ as the pitch-angle-dependent cross-field diffusion coefficient (CFDC), $\hat{\boldsymbol{b}} = \boldsymbol{B}/B$ as a unit vector in the direction of the background magnetic field, and I as the 3×3 identity matrix. The terms in Eq. 1, from left to right, describe temporal changes, the motion of the instantaneous guiding centre (GC), momentum and pitch-angle changes due to pseudo-forces arising from measuring momentum in the non-inertial frame of the plasma flow, and pitch-angle and spatial diffusion, respectively. The assumption that perpendicular diffusion is the same in both directions perpendicular to the magnetic field in the diffusion tensor is only valid for axisymmetric turbulence. We assumed that the mixed spatial and pitch-angle diffusion coefficients (i.e. $D_{\mu\perp}$ and $D_{\perp\mu}$) are negligible. This is a simplification, but according to Schlickeiser (2011), these terms vanish for incompressible, axisymmetric turbulence.

Furthermore, in Eq. 1,

$$\boldsymbol{v}_{\mathrm{gc}} = \mu v \hat{\boldsymbol{b}} + \boldsymbol{u} + \boldsymbol{v}_{\mathrm{d}}(\mu), \tag{2a}$$

$$\frac{\mathrm{d}p}{\mathrm{d}t} = p\left\{\frac{1-3\mu^2}{2}\hat{\boldsymbol{b}}\hat{\boldsymbol{b}} : \boldsymbol{\nabla}\boldsymbol{u} - \frac{1-\mu^2}{2}\boldsymbol{\nabla}\cdot\boldsymbol{u} - \frac{\mu}{v}\hat{\boldsymbol{b}}\cdot\left[\frac{\partial \boldsymbol{u}}{\partial t} + (\boldsymbol{u}\cdot\boldsymbol{\nabla})\,\boldsymbol{u}\right]\right\}, \tag{2b}$$

$$\frac{\mathrm{d}\mu}{\mathrm{d}t} = \frac{1-\mu^2}{2}\left\{v\,\boldsymbol{\nabla}\cdot\hat{\boldsymbol{b}} + \mu\,\boldsymbol{\nabla}\cdot\boldsymbol{u} - 3\mu\,\hat{\boldsymbol{b}}\hat{\boldsymbol{b}} : \boldsymbol{\nabla}\boldsymbol{u} - \frac{2}{v}\hat{\boldsymbol{b}}\cdot\left[\frac{\partial \boldsymbol{u}}{\partial t} + (\boldsymbol{u}\cdot\boldsymbol{\nabla})\,\boldsymbol{u}\right]\right\}, \tag{2c}$$

with v as the particle speed in the flow frame, $\boldsymbol{u}$ as the flow velocity, $\boldsymbol{v}_{\mathrm{d}}(\mu)$ as the gyrophase-averaged GC drift velocity in the flow frame, and $\boldsymbol{ab} : \boldsymbol{cd} = a_i b_j c_j d_i$ indicating a tensor contraction. The motion of the GC, described by the terms in Eq. 2a from left to right, includes streaming of GCs along the magnetic field, advection by the plasma flow in which the magnetic field is embedded, and drifts of the GCs relative to the magnetic field. The drift velocity, $\boldsymbol{v}_{\mathrm{d}}(\mu)$, is mainly due to GC drift perpendicular to the background magnetic field, but there may also be some drift

[1] One can observe non-zero magnetic or cross helicities in the inner heliosphere (see e.g. Breech et al. 2005), but we do not consider this further (see Schlickeiser 2002 for how non-zero helicities lead to asymmetric PADCs).

along the field (see Rossi & Olbert 1970 and Burger et al. 1985 for a discussion). The momentum changes in Eq. 2b include the inverse Fermi and betatron effects (the first two terms; see Webb & Gleeson 1979) and the acceleration of the flow (the last two terms). These pseudo-forces are also included in Eq. 2c for pitch-angle changes, with magnetic mirroring or focusing due to a gradient along the magnetic field also contributing (the first term). Webb & Gleeson (1979), Ruffolo (1995), le Roux et al. (2007), Lampa (2011), and le Roux & Webb (2012) provide detailed interpretations and discussions of the various physical processes included in the FTE, with van den Berg (2023) giving a summary. Both Eqs 2b and 2c could also include terms arising from an electric field aligned with the magnetic field, which the transformation into the flow frame might not remove (Zhang 2006; le Roux & Webb 2012). However, it is usually assumed that the SW is infinitely conductive, so that there are no large-scale field-aligned electric fields. The dependence of all these terms on the pitch cosine implies that the pitch angle not only governs the efficiency of spatial transport but also energy changes.

The Parker TPE can be derived from the FTE using a perturbation approach, assuming the distribution is nearly isotropic. Through an arduous mathematical process (see Hasselmann & Wibberenz 1970; Schlickeiser 2002; Litvinenko & Schlickeiser 2013; He & Schlickeiser 2014; van den Berg 2023), this derivation requires that pitch-angle scattering be efficient enough to keep the distribution nearly isotropic, implying that deterministic pitch-angle changes must be negligible (formally, by setting $\mathrm{d}\mu/\mathrm{d}t = 0$); that all other physical processes (i.e. perpendicular diffusion, advection, drifts, and momentum changes) be slower than or unimportant compared with parallel diffusion; and that there be no interplay between pitch-angle scattering and perpendicular diffusion. This then yields the pitch-angle-independent quantities,

$$F_0 = \frac{1}{2}\int_{-1}^{1} f(\mu)\,\mathrm{d}\mu, \tag{3a}$$

$$\boldsymbol{V}_\mathrm{d} = \frac{1}{2}\int_{-1}^{1} \boldsymbol{v}_\mathrm{d}(\mu)\,\mathrm{d}\mu, \tag{3b}$$

$$\frac{1}{2}\int_{-1}^{1} \frac{\mathrm{d}p}{\mathrm{d}t}\,\mathrm{d}\mu = -\frac{p}{3}\left(\boldsymbol{\nabla}\cdot\boldsymbol{u}\right), \tag{3c}$$

$$\kappa_\parallel = \frac{v^2}{8}\int_{-1}^{1} \frac{(1-\mu^2)^2}{D_{\mu\mu}(\mu)}\,\mathrm{d}\mu, \tag{3d}$$

$$\kappa_\perp = \frac{1}{2}\int_{-1}^{1} D_\perp(\mu)\,\mathrm{d}\mu, \tag{3e}$$

to be used in the Parker TPE, with $\kappa_\parallel$ and $\kappa_\perp$ as the isotropic DCs parallel and perpendicular to the background magnetic field, respectively. If focusing or mirroring is included in this derivation (by keeping only the first term in Eq. 2c; see Beeck & Wibberenz 1986; Litvinenko & Schlickeiser 2013; He & Schlickeiser 2014; Wang & Qin 2018; van den Berg 2023), the definitions of the DCs change to include the so-called focusing length,[2] $L^{-1} = \boldsymbol{\nabla}\cdot\hat{\boldsymbol{b}}$, and additional advection terms arise from the interplay between scattering and focusing (not shown here). This, in turn, requires that $\lambda_\parallel \ll |L|$ to keep the distribution nearly isotropic, where $\lambda = 3\kappa/v$ is the particle MFP. Additional correction terms enter the TPE when the perturbation is not small (see He & Schlickeiser 2014; Wang & Qin 2018). However, these correction terms seem to vanish for a constant focusing length, are of fourth order in $\lambda_\parallel/|L|$ for a spatially varying focusing length and isotropic pitch-angle scattering in the weak focusing limit (He & Schlickeiser 2014), and only seem to modify the parallel DC as long as pitch-angle scattering, perpendicular diffusion, and the focusing length are constant in space (Wang & Qin 2018).

The first requirement (that $\mathrm{d}\mu/\mathrm{d}t = 0$ or that $\lambda_\parallel \ll |L|$) holds for high-energy particles in the outer heliosphere, but not over the poles, where magnetic focusing may still be significant relative to large parallel MFPs. The second requirement (that parallel diffusion must be the fastest process) implies that either $\kappa_\perp \ll \kappa_\parallel$, or that the distribution should not exhibit large gradients perpendicular to the magnetic field (since perpendicular diffusive transport is proportional to both the CFDC and the perpendicular gradient). Although $\kappa_\perp/\kappa_\parallel$ is sensitive to the predictions of the employed scattering theories and to the turbulence transport models used as input to those theories (see e.g. Engelbrecht et al. 2022a), it is generally slightly larger over the poles than in the equatorial regions (see e.g. Engelbrecht & Burger 2013a,b; Moloto et al. 2018) and might approach a sizeable fraction of one in the outer heliosphere, depending on how the effect of pick-up-ion-generated turbulence is incorporated into the parallel MFP (compare Engelbrecht 2017; Zhao et al. 2017). At least galactic protons do not exhibit large spatial variation between 0.4 – 2 GV (0.082 – 1.27 GeV), as their radial and latitudinal gradients are less than $\sim 4\%\ \mathrm{au}^{-1}$ and $\sim 0.2\%\ \mathrm{deg}^{-1}$, respectively (see Rankin et al. 2022, and references therein). The last requirement (that there should be no interplay between pitch-angle scattering and perpendicular diffusion) implies that perpendicular diffusion must be independent of pitch angle. However, limited full-orbit simulations (see Qin & Shalchi 2014) and theoretical considerations (see Strauss et al. 2016; Engelbrecht 2019) indicate that this is not the case.

From these considerations, one can conclude that GCR transport may exhibit subtleties beyond the assumption of isotropy, especially in the polar regions of the heliosphere. In contrast, the classical derivation of the Parker TPE, which starts from a continuity equation (i.e. Parker 1965; Jokipii & Parker 1970; Webb & Gleeson 1979; Moraal 2013), seems to imply that the Parker TPE is valid for an isotropic distribution, with position and time measured in a stationary observer's frame and momentum measured in a non-relativistic flow frame. These derivations also do not theoretically derive the form of the diffusion tensor but rather justify it by the empirical observation that particles diffuse both parallel and perpendicular to the magnetic field. It is also usually assumed that $\kappa_\parallel \gg \kappa_\perp$, based on some physical considerations (see e.g. Parker 1965, 1967; Jokipii & Parker 1970), which is also justified by theory, observations, and test-particle simulations (see e.g. Shalchi 2020; Engelbrecht et al. 2022a; Lang et al. 2024; Els et al. 2024). This classical derivation is less revealing about the restrictions on the Parker TPE and its application, as it does not necessarily make explicit the underlying assumptions required to derive the Parker TPE from the FTE.

The Parker TPE is an evolution equation for the omnidirectional intensity, $F_0(\boldsymbol{r}, p, t)$, of the particle number density per unit momentum volume, with momentum measured in the flow frame. It is given by (Jokipii & Parker 1970; Webb & Gleeson

[2] The inclusion of an electric field parallel to the magnetic field would also cause an anisotropic distribution, with the electric field playing a role analogous to focusing.

1979; Moraal 2013)

$$\frac{\partial F_0}{\partial t} + \nabla \cdot [(\boldsymbol{u} + \boldsymbol{V}_\mathrm{d}) F_0] - \frac{1}{p^2}\frac{\partial}{\partial p}\left[p^2 \frac{p}{3}(\nabla \cdot \boldsymbol{u}) F_0\right]$$
$$= \nabla \cdot (\kappa \cdot \nabla F_0), \tag{4}$$

where $\kappa = \kappa_\parallel \hat{\boldsymbol{b}}\hat{\boldsymbol{b}} + \kappa_\perp(\mathrm{I} - \hat{\boldsymbol{b}}\hat{\boldsymbol{b}})$ is the isotropic diffusion tensor for axisymmetric turbulence. The terms in Eq. 4, from left to right, describe temporal changes, advection by the plasma flow, drifts of the GC relative to the magnetic field, adiabatic energy changes, and spatial diffusion, respectively. Note that momentum diffusion can also be included (see e.g. Quenby 1984; Schlickeiser 2002), that the drift velocity can be absorbed into the diffusion tensor if it is divergence-free (see e.g. Jokipii & Parker 1970; Minnie et al. 2007), and that the form of the TPE differs when working in a stationary observer's frame (as is also the case for the FTE; see Webb & Gleeson 1979). Although momentum diffusion may be important for certain applications, such as anomalous CRs (see e.g. Strauss et al. 2010, 2011), it is a second-order process in the flow frame and is usually neglected in GCR transport because diffusion, adiabatic energy changes, and drifts are more important for high-energy GCRs (hence its neglect in the FTE as well).

Deriving the Parker TPE from the FTE yields some interesting insights, as van den Berg (2023) discusses. Firstly, to the lowest order, anisotropy arises from a local balance among pitch-angle scattering, focusing, and the momentum and spatial gradients of F_0, which act as source terms (see also Hasselmann & Wibberenz 1970). This implies that the absence of focusing or field-aligned electric fields does not guarantee an isotropic CR distribution. Secondly, Eq. 3c implies that particles undergo some energy changes that should average out for an isotropic distribution, but the adiabatic energy change in the Parker TPE would be only an approximation if any process causes an anisotropic distribution. Hence, the Parker TPE may under- or overestimate CR energy losses if the distribution is anisotropic. Although we do not specify the exact forms of $\boldsymbol{v}_\mathrm{d}(\mu)$ and $\boldsymbol{V}_\mathrm{d}$ here, as this paper focuses on diffusion, one can draw a similar conclusion from Eq. 3b about the drift terms. However, the effect of this on CR modulation is unclear, as Burger et al. (1985), for example, concluded that the isotropic drift velocity could still be acceptable even if 95% of the particles propagate in the same direction, with half of them having $|\mu| > 0.72$. Thirdly, the parallel diffusion term of Eq. 3d follows from the streaming term ($\mu v \hat{\boldsymbol{b}}$; hence its explicit inclusion in Eq. 2a) and the pitch-angle diffusion term, indicating that parallel spatial diffusion arises from pitch-angle scattering that disrupts particle streaming along the field (see also van den Berg et al. 2020). Hence, a larger parallel DC, due to reduced pitch-angle scattering, actually implies more streaming, which is a non-diffusive process. The Parker TPE might therefore be only an approximation for CR transport in the outer heliosphere and over the poles, where the parallel MFP is generally expected to be very large (see again Engelbrecht & Burger 2013a,b; Zhao et al. 2017; Moloto et al. 2018; Engelbrecht et al. 2022a). Fourthly, including the interplay between pitch-angle scattering and other pitch-angle-dependent processes would introduce additional diffusion and advection terms in both momentum and configuration space (see the discussion and summary in van den Berg 2023). One could argue that the community should revise the definitions of the parallel and perpendicular MFPs to account for these additional spatial DCs. Moreover, pitch-angle scattering and perpendicular diffusion might be coupled and cannot be treated separately: this is not merely a case of parallel and perpendicular diffusion being dependent on one another (see the theories of Matthaeus et al. 2003; Qin 2007; Shalchi 2010), but also of missing diffusion terms in the Parker TPE. Lastly, any process that produces an anisotropic distribution would modify the definition of the MFPs, depending on the pitch-angle dependence of the PADC and CFDC (e.g. a distribution with more field-aligned particles would have a larger parallel MFP since $D_{\mu\mu} \propto 1 - \mu^2$ in general). Taken together, this and the previous realisation imply that any parallel (perpendicular) DC inferred from fitting the Parker TPE to observations is an 'effective parallel (perpendicular) DC' that includes diffusion contributions from all physical processes, not just from pitch-angle scattering (cross-field diffusion).

Since the Parker TPE follows from the FTE, one should also consider the limitations of the FTE for transparency. Firstly, the inclusion of perpendicular transport (i.e. drifts and cross-field diffusion) in the FTE has been questioned, as summarised by van den Berg et al. (2020), because all spatial transport across the magnetic field is absent from the original derivations (see e.g. Skilling 1971; Isenberg 1997; Zank 2014). However, le Roux et al. (2007) showed that drift effects persist in the momentum changes, and alternative derivations (see Schlickeiser 2002; Zhang 2006; Wijsen 2020) show that perpendicular transport can be retained if one transforms to the GC position before performing a gyrophase average (see van den Berg 2023 for a possible explanation of why this is). It is ironic, then, that the inclusion of perpendicular transport in the Parker TPE has not been questioned to the same extent as in the FTE. The FTE with perpendicular transport, and by implication the Parker TPE, is valid only when working with GCs, but the inclusion of perpendicular transport need not be questioned. However, one should exercise caution when the fields vary over distances smaller than the Larmor radius, as the instantaneous GC velocity is not relativistically consistent (see the discussions by Isenberg & Jokipii 1979; Burger et al. 1985). Secondly, just as isotropy is the limiting factor for the Parker TPE, the FTE assumes a gyrotropic distribution. le Roux et al. (2014) showed that a non-uniform magnetic field or flow, an accelerating flow, or an electric field could cause slow variations in the gyrophase (processes that are especially important at perpendicular shocks), which might lead to a non-gyrotropic distribution. Additionally, Wijsen (2020) points out that neutral sheet drift could also produce a non-gyrotropic distribution. As with all models, some approximations are necessary to keep the problem tractable, and the gyrotropic assumption appears unavoidable to avoid solving a much more complicated gyrophase TPE. Lastly, the most technical assumption is that both the Parker and focused TPEs assume diffusive behaviour. This implies that one must consider the evolution of the distribution over a time interval that is short enough for the distribution not to change significantly, but not so short that the microphysical processes are quasi-deterministic (in light of the gyrotropic assumption, this implies that for the FTE, the pitch-angle decorrelation time should be longer than the cyclotron period; see e.g. Hasselmann & Wibberenz 1970; Schlickeiser 2002; Zank 2014; van den Berg 2023). The assumption of diffusive pitch-angle scattering in the FTE, however, is less restrictive than that of diffusive spatial transport in the Parker TPE since the FTE still allows particle streaming along the magnetic field (see e.g. Effenberger et al. 2025 for a review of non-diffusive transport and its applications). Although the limitations of the FTE are real and one should heed them, they are on a different physical level from those of the Parker TPE, so that the FTE is the more complete TPE.

3. Numerical method

We must specify the flow velocity, HMF, and DCs to apply Eqs 1 or 4 to a particular scenario. Fortunately, because GCRs are quasi-stationary (i.e. their intensities change over long time intervals), we need not consider the temporal evolution of the TPEs. We chose the DCs and heliospheric structure to represent those typically used successfully in GCR modulation studies at solar minimum. These are similar to those of Vos (2011) and Raath (2015), with specific modifications introduced to simplify the problem and reduce computational complexity. Many aspects of these models are also discussed in Potgieter (2013) and utilised in numerous other works. Although these DCs are somewhat arbitrary, prior studies have shown that they reproduce GCR observations at Earth without unnecessary complexity. The parameters used in this study are the averages of those employed by Vos (2011) and Potgieter et al. (2014) to replicate the proton observations made by the Payload for Antimatter Matter Exploration and Light-nuclei Astrophysics experiment between 2006 and 2009 (see also Raath 2015).

3.1. Heliospheric structure and diffusion coefficients

Following Gleeson & Urch (1971), we required the flux through the solar surface at a radial distance of $r_\odot = 0.005$ au to be zero. This implies a reflective inner boundary if the SW speed is zero at the solar surface and if drifts are neglected. We placed an outer boundary at a radial distance of $R_\mathrm{o} = 90$ au to avoid complications arising from pitch-angle-dependent diffusive shock acceleration and a potentially non-gyrotropic distribution at the termination shock (see e.g. le Roux et al. 2007, 2014). Here, we assumed that GCRs enter the modulation cavity isotropically (i.e. uniformly across latitude, longitude, and pitch cosine, with μ uniformly distributed between $[-1;1]$). We specified the spectrum of GCR protons from Vos (2011) here as a function of kinetic energy K by

$$j_\mathrm{o}(K) = \#\ \mathrm{m}^{-2}\ \mathrm{s}^{-1}\ \mathrm{sr}^{-1}\ \mathrm{MeV}^{-1} \begin{cases} 0.8\,\mathrm{e}^{4.64-0.08[\ln(K/K_\mathrm{r})]^2-2.91\sqrt{K/K_\mathrm{r}}} & \text{if} \quad K < 1.4\ \mathrm{GeV} \\ 0.775\,\mathrm{e}^{3.22-2.78\ln(K/K_\mathrm{r})-1.5(K_\mathrm{r}/K)} & \text{if} \quad K \geq 1.4\ \mathrm{GeV} \end{cases}, \tag{5}$$

where the differential intensity is related to the omnidirectional intensity by $j_K = p^2 F_0/2$ (see Moraal 2013 for useful relations among different quantities) and $K_\mathrm{r} = 1$ GeV. Note that this so-called very-local interstellar spectrum is usually specified at a radial distance of ~ 120 au, implying that the current model would yield too high intensities because modulation in the heliosheath (see e.g. Stone et al. 2013) and by the termination shock is absent here. The aim of the present study, however, is not to reproduce a specific set of observations but rather to compare the results obtained from the Parker and focused TPEs using a set of commonly used transport coefficients.

We neglected drifts (i.e. $\boldsymbol{v}_\mathrm{d}(\mu) = \mathbf{0}$ and $\boldsymbol{V}_\mathrm{d} = \mathbf{0}$) in this initial study for simplicity and to systematically characterise the effects of different physical processes on any differences that may be observed in the results of the Parker and focused TPEs. The GC velocity being relativistically inconsistent and the potential departure from a gyrotropic distribution due to neutral sheet drift, as discussed in Sect. 2, are additional considerations for neglecting drifts here. We computed the stationary solutions of Eqs 1 and 4 (i.e. with $\partial f/\partial t = 0$ and $\partial F_0/\partial t = 0$, respectively) in a reference frame co-rotating with the Sun (we also present the results in Sect. 4 in this frame). This specifies the flow velocity as

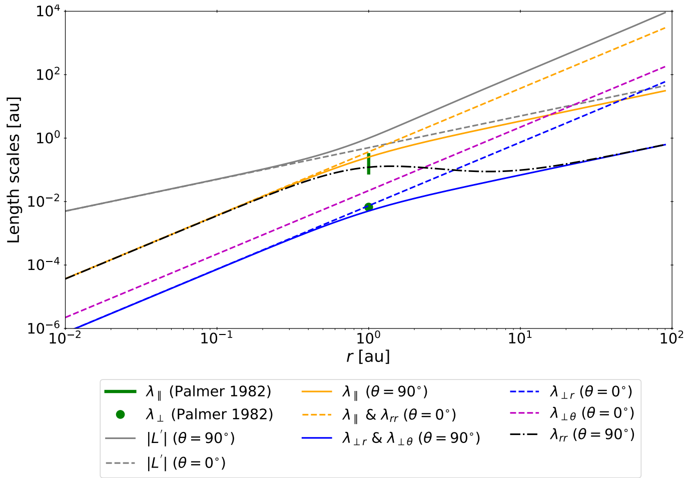

Fig. 1: Modified focusing length (Eq. 11; grey lines) and various MFPs for 1 GeV protons as a function of radius in the equatorial plane (solid lines) and at the poles (dashed lines). The dashed orange line represents both $\lambda_\parallel$ and λ_{rr} over the poles, whereas these two quantities differ in the equatorial plane (solid orange and dash-dotted black lines, respectively). Similarly, the solid blue line represents both $\lambda_{\perp r}$ and $\lambda_{\perp\theta}$ in the equatorial plane, whereas these two quantities differ over the poles (dashed blue and magenta lines, respectively). Lower-energy (higher-energy) particles have smaller (larger) MFPs. For this particle energy, $L' \approx L$ because the additional term in L' is of the second order in v_sw/v. The green vertical line and dot indicate the Palmer (1982) consensus values at Earth for reference.

(Parker 1958; Vos 2011)

$$\boldsymbol{u} = v_\mathrm{sw}(r,\theta)\,(\hat{\boldsymbol{r}} - \tan\psi\,\hat{\boldsymbol{\phi}}), \tag{6}$$

where $\tan\psi = \omega_\odot(r - r_\odot)\sin\theta/v_\mathrm{sw}$ specifies the spiral angle (the angle between the HMF line and the radial direction), with $\omega_\odot = 2\pi/(25.4\ \text{days}) = 1.03\times10^{-2}$ rad h^{-1} as the solar rotation rate and $\hat{\boldsymbol{r}}$ and $\hat{\boldsymbol{\phi}}$ as unit vectors in the radial and azimuthal direction, respectively. The Parker (1958) HMF is valid in such a frame and is given by

$$\boldsymbol{B} = B_\mathrm{P}\left(\frac{r_\oplus}{r}\right)^2 (\hat{\boldsymbol{r}} - \tan\psi\,\hat{\boldsymbol{\phi}}), \tag{7}$$

where $B_\mathrm{P} = B_\oplus/\sqrt{1+\omega_\odot^2(r_\oplus - r_\odot)^2/V_\mathrm{sw}^2}$ is normalised to the HMF magnitude at Earth (i.e. $B_\oplus = 4.44$ nT at $r_\oplus = 1$ au; see Owens & Forsyth 2013 for a summary of the Parker HMF). We assumed that the SW is radially directed, accelerates near the Sun from 0 km s^{-1} to a constant value of $V_\mathrm{sw} = 400$ km s^{-1} in the equatorial region (in accordance with Sheeley et al. 1997), and is twice as fast over the poles (in accordance with McComas et al. 2000). We parametrised this by

$$v_\mathrm{sw} = V_\mathrm{sw}\,\frac{1-\mathrm{e}^{\eta(1-r/r_\odot)}}{2}\left[3+\tanh\left(\frac{|\theta-90°|-\alpha_\odot-\theta_\mathrm{s}}{\theta_\mathrm{t}}\right)\right], \tag{8}$$

where $\eta = 1/15$ governs the radial transition rate, $\alpha_\odot = 13.5°$ is the tilt angle between the magnetic and rotation axis of the Sun[3], $\theta_\mathrm{s} = 15°$, and $\theta_\mathrm{t} = 45°/2\pi$ governs the latitudinal transition

[3] Although we did not include a heliospheric current sheet in the model, $\alpha_\odot$ is usually between $\sim 5°$ and $\sim 20°$ during solar-minimum conditions, such that $\alpha_\odot + \theta_\mathrm{s} \sim 30°$ in most modulation studies (see Vos 2011; Potgieter 2013; Potgieter et al. 2014; Raath 2015).

rate (the expressions of Vos 2011, Potgieter 2013, Potgieter et al. 2014, and Raath 2015 have similar functional forms that differ slightly in numerical values).

We specified the parallel DC as a function of rigidity P by

$$\kappa_{\|} = \kappa_0 \, \frac{vB_0}{cB} \left(\frac{P}{P_{\rm r}}\right)^{\rho} \left[\frac{(P/P_{\rm r})^{\gamma} + (P_{\rm k}/P_{\rm r})^{\gamma}}{1 + (P_{\rm k}/P_{\rm r})^{\gamma}}\right]^{\frac{\delta-\rho}{\gamma}}, \tag{9}$$

where $\kappa_0 = 1.3 \times 10^{23}$ cm^2 s^{-1} = 2.1 au^2 h^{-1}, B_0 = 1 nT, c is the speed of light in vacuum, $P_{\rm r}$ = 1 GV (= 0.43 GeV for protons), $P_{\rm k}$ = 4 GV (= 3.17 GeV for protons) is the rigidity where the break in the power law from low energies with index $\rho = 0.43$ to high energies with index $\delta = 1.95$ occurs, and $\gamma = 3$ governs the smoothness of the power law transition (Vos 2011; Potgieter 2013; Potgieter et al. 2014; Raath 2015). We show the equivalent parallel MFP for a 1 GeV proton in Fig. 1. Its value at Earth falls within the upper range of the Palmer (1982) consensus values (vertical green line). The magnetic field strength determines the spatial dependence of the DC, causing the parallel MFP to increase $\propto r^2$ over the poles (dashed orange line) and for $r < 1$ au, while the parallel MFP increases $\propto r$ in the equatorial plane for $r > 1$ au (solid orange line). This parallel DC has an energy dependence comparable to that of the magnetostatic quasi-linear theory (QLT), which predicts $\lambda_{\|} \propto P^{1/3}$ at low energies, and $\lambda_{\|} \propto P^2$ at high energies. However, the assumed spatial behaviour of various turbulence quantities governs the spatial dependence of the QLT parallel MFP (see e.g. the expression of Burger et al. 2008), and combining turbulence transport models with the QLT expression usually produces a stronger radial variation than observed in Fig. 1 (see the summary in Engelbrecht et al. 2022a).

We set the CFDC in the cone containing the HMF spiral to some fraction $\chi = 0.02$ of the parallel DC (in accordance with Giacalone & Jokipii 1999), while we enhanced the CFDC in the polar direction by a factor of $\varsigma = 3$ over the poles (in accordance with Burger et al. 2000; Ferreira et al. 2001) and gave it the same latitudinal dependence as the SW for both simplicity and consistency (in contrast to Vos 2011, Potgieter 2013, Potgieter et al. 2014, and Raath 2015, who use slightly different latitudinal dependencies for the SW and perpendicular DC). We parametrised this by

$$\kappa_{\perp r} = \chi \, \kappa_{\|}, \tag{10a}$$

$$\kappa_{\perp\theta} = \kappa_{\perp r} \left[\frac{\varsigma + 1}{2} + \frac{\varsigma - 1}{2} \tanh\left(\frac{|\theta - 90°| - \alpha_{\odot} - \theta_{\rm s}}{\theta_{\rm t}}\right)\right], \tag{10b}$$

and relaxed the assumption of axisymmetric perpendicular diffusion.[4] Figure 1 shows that the perpendicular MFPs of a 1 GeV proton are equal in the equatorial plane (solid blue line) along the radial and polar directions, but differ in magnitude over the poles (dashed blue and magenta lines). At Earth, the perpendicular MFP is slightly smaller than the Palmer (1982) consensus value (green dot). Note that the perpendicular DCs share the same spatial and energy dependencies as the parallel DC. This is only somewhat reminiscent of the theoretical expression derived from the non-linear guiding centre (NLGC) theory (see e.g. the expression of Burger et al. 2008), which has a weaker $\lambda_{\perp} \propto \lambda_{\|}^{1/3}$ dependence and would therefore exhibit a less pronounced spatial and energy dependence (not taking into account the spatial dependence of the turbulence quantities; see the discussion of Engelbrecht et al. 2022a).

Figure 1 also shows a modified focusing length,

$$L^{'-1} = \boldsymbol{\nabla} \cdot \hat{\boldsymbol{b}} - \frac{2}{v^2} \, \hat{\boldsymbol{b}} \cdot \left[\frac{\partial \boldsymbol{u}}{\partial t} + (\boldsymbol{u} \cdot \boldsymbol{\nabla}) \, \boldsymbol{u}\right], \tag{11}$$

which no study has considered previously but is more generally applicable in the heliosphere, as only the $\mu\left(\boldsymbol{\nabla} \cdot \boldsymbol{u} - 3 \, \hat{\boldsymbol{b}}\hat{\boldsymbol{b}} : \boldsymbol{\nabla}\boldsymbol{u}\right)$ terms are neglected in Eq. 2c when deriving the Parker TPE from the FTE. We considered this form for completeness, although it generally represents the HMF focusing effect for the particle energies considered here, because the additional term is of the second order in $v_{\rm sw}/v$ (which is $\sim 0.67 - 1.33 \times 10^{-2}$ for the lowest energies considered). The diffusion condition ($\lambda_{\|} < |L^{'}|$) is met in the equatorial region (compare the solid orange and grey lines), but not over the poles (compare the dashed orange and grey lines). The ratio of $\lambda_{\|}$ to $|L^{'}|$ grows $\propto r$ from $\sim 7 \times 10^{-3}$ to ~ 0.3 at $r \approx 0.7$ au in the equatorial plane and then decreases $\propto r^{-1}$ to $\sim 3 \times 10^{-3}$ at the outer boundary. Over the poles, $\lambda_{\|}/|L^{'}|$ increases linearly with radial distance, reaching $\sim$ 70 at the outer boundary. Although the focusing length is large in the outer heliosphere, the violation of the diffusion condition over the poles is mostly due to very large parallel MFPs (i.e. a combination of $|L^{'}| \propto r$ and $\lambda_{\|} \propto r^2$).

The FTE requires pitch-angle-dependent DCs, which we normalised in this study to the parallel and perpendicular DCs using Eqs 3d and 3e, respectively. This enabled a direct, consistent comparison of results between the Parker and focused TPEs. We investigated both isotropic and anisotropic pitch-angle scattering (not to be confused with isotropic or anisotropic distributions). We parametrised the two PADCs by

$$D_{\mu\mu}^{\rm iso}(\mu) = D_{\rm I} \, (1 - \mu^2), \tag{12a}$$

$$D_{\mu\mu}^{\rm aniso}(\mu) = D_{\rm A} \, (1 - \mu^2) \left(\frac{|\mu|}{1 + |\mu|} + \epsilon\right), \tag{12b}$$

respectively, where $D_{\rm I} = v^2/6\kappa_{\|}$,

$$D_{\rm A} = \frac{v^2}{4\kappa_{\|}(1+\epsilon)^4} \left[\frac{1}{6} + 2\epsilon + \frac{5}{2}\epsilon^2 + \frac{2}{3}\epsilon^3 + (1 + 2\epsilon) \ln\left(\frac{1 + 2\epsilon}{\epsilon}\right)\right] \tag{13}$$

for $\epsilon \neq 0$, and $\epsilon = 0.045$ parametrises dynamical effects. We used the anisotropic PADC of Agueda et al. (2008) here because its derivative is well behaved around $\mu = 0$ (see Agueda & Vainio 2013 for the normalisation). We calculated both $D_{\rm I}$ and $D_{\rm A}$ from Eq. 9, using Eq. 3d, to ensure that parallel diffusion is consistent across the Parker and focused TPEs. An anisotropic PADC (Eq. 12b) is consistent with dynamical QLT and is commonly used in the FTE, whereas an isotropic PADC (Eq. 12a) would be expected only in strong turbulence or in magnetostatic QLT for particles resonating with a turbulence spectrum inversely proportional to the parallel wavenumber (i.e. $k_{\|}^{-1}$). We compactly wrote the CFDC as

$$D_{\perp}(\mu) = h(\mu) \, \kappa_{\perp}, \tag{14}$$

where $h(\mu)$ governs the pitch-angle dependence and normalisation. We used pitch-angle-independent perpendicular diffusion with $h(\mu) = 1$ when employing Eq. 12a, and $h(\mu) = 3\mu^2$, representing non-linear theories (see Qin & Shalchi 2014;

[4] Theory shows that non-axisymmetric turbulence leads to an increase in the perpendicular DC in one transverse direction and a corresponding decrease in the other (see e.g. Ruffolo et al. 2006, 2008; Strauss et al. 2016). This effect, however, is usually ignored in modulation studies using non-axisymmetric perpendicular DCs, and we did so too.

Engelbrecht 2019), when employing Eq. 12b. To ensure that perpendicular diffusion is consistent across the Parker and focused TPEs, we calculated the numerical factor in $h(\mu)$ from Eq. 10, using Eq. 3e. The choice of isotropic pitch-angle scattering with pitch-angle-independent perpendicular diffusion is the simplest option for the FTE, as there is no interplay between pitch-angle scattering and cross-field diffusion. The choice of anisotropic pitch-angle scattering with pitch-angle-dependent perpendicular diffusion represents a more realistic situation (i.e. dynamical QLT for the PADC and NLGC theory for the CFDC; see e.g. Schlickeiser 2002; Engelbrecht 2019).

3.2. Stochastic differential equations

As explained by Strauss & Effenberger (2017), the stationary solution for GCRs is easiest to compute using time-backward stochastic differential equations (SDEs). The general backward Kolmogorov equation is of the form

$$-\frac{\partial \tilde{P}}{\partial \tau} = \boldsymbol{a} \cdot \boldsymbol{\nabla}_{\boldsymbol{q}} \tilde{P} + \frac{1}{2} \mathsf{C} : \boldsymbol{\nabla}_{\boldsymbol{q}} \boldsymbol{\nabla}_{\boldsymbol{q}} \tilde{P} - Ł\tilde{P}, \tag{15}$$

where $\tau = T - t$ is a backward time coordinate starting at some final time $t = T$, $\boldsymbol{q}$ is an n-dimensional vector with generalised (i.e. phase-space) coordinates, $\boldsymbol{\nabla}_{\boldsymbol{q}}$ is the gradient operator in n-dimensional phase space, $\tilde{P}(\boldsymbol{q}, \tau \,|\, \boldsymbol{q}_\mathrm{f}, 0)$ is the conditional probability from a final state $\boldsymbol{q}_\mathrm{f}$ at time $t = T$ ($\tau = 0$), $\boldsymbol{a}(\boldsymbol{q}, \tau)$ is an n-dimensional vector describing drifts in phase space (not to be confused with the physical particle drift process), $\mathsf{C}(\boldsymbol{q}, \tau)$ is an $n \times n$ matrix describing diffusion in phase space (also not to be confused with the physical particle diffusion process), and $Ł(\boldsymbol{q}, \tau)$ is the linear coefficient. The Itô-type SDE equivalent to this equation is

$$\mathrm{d}\boldsymbol{Q}(\tau) = \boldsymbol{a}(\boldsymbol{Q}, \tau)\,\mathrm{d}\tau + \mathsf{B}(\boldsymbol{Q}, \tau) \cdot \mathrm{d}\boldsymbol{W}(\tau), \tag{16}$$

where $\boldsymbol{Q}(\tau) = \boldsymbol{q}(\tau)$ are random variables corresponding to $\boldsymbol{q}$ (this relation implies that the variable $\boldsymbol{q}$, called a deterministic variable, is changing randomly, and it is this stochastic nature that $\boldsymbol{Q}$ models), $\mathsf{C} = \mathsf{B} \cdot \mathsf{B}^\mathrm{T}$, and $\mathrm{d}\boldsymbol{W}(\tau)$ are n independent Wiener processes (i.e. time-stationary stochastic Lévy processes where the time increments have a normal distribution with a mean of zero and a variance of $\mathrm{d}\tau$). In the modelling community, the temporal evolution of $\boldsymbol{Q}$ is called the 'trajectory of a pseudo-particle'. However, 'the temporal evolution of a phase-space density element' would be a more apt description, as the TPE describes the temporal evolution of a phase-space density element within an ensemble. A pseudo-particle trajectory represents only one possible realisation of how a pseudo-particle might evolve. One should therefore use an ensemble of solutions (each independent of the others if the stochastic drift and diffusion coefficients are independent of the distribution function) to statistically compute quantities of interest, such as GCR differential intensities. The time-backward approach described here is mathematically equivalent to a time-forward approach in the stationary limit. However, the time-backward approach is computationally more efficient because it ensures that all pseudo-particles contribute to the answer at the observer (Gardiner 1994; Kloeden & Platen 1995; Kopp et al. 2012; Strauss & Effenberger 2017).

The trajectory of the pseudo-particle was computed iteratively using the Euler-Maruyama scheme, i.e.

$$\begin{aligned} \boldsymbol{Q}(\tau_k + \Delta\tau_k) \approx\ & \boldsymbol{Q}(\tau_k) + \boldsymbol{a}(\boldsymbol{Q}(\tau_k), \tau_k)\,\Delta\tau_k\ + \\ & \mathsf{B}(\boldsymbol{Q}(\tau_k), \tau_k) \cdot \boldsymbol{\Lambda}(\tau_k)\,\sqrt{\Delta\tau_k}, \end{aligned} \tag{17}$$

where $\Delta\tau_k$ is the time step of the k^th iteration, $\tau_k = \sum_{l=1}^{k} \Delta\tau_l$, and $\boldsymbol{\Lambda}(\tau_k)$ are n independent normally distributed pseudo-random numbers with zero mean and unit variance (Kloeden & Platen 1995; Strauss & Effenberger 2017). We generated uniformly distributed pseudo-random numbers on $[0; 1]$ using the permuted congruential generator of O'Neill (2014)[5] and transformed them into normally distributed random numbers for the Wiener process via the Box-Muller transformation (see Press et al. 1992). Following Strauss & Effenberger (2017), we handled the linear term in Eq. 15 by assigning a weight, w, to the pseudo-particle, which implies that

$$\begin{aligned} & \frac{\partial \tilde{P}}{\partial \tau} \propto Ł\tilde{P} \\ \Longrightarrow\quad & \mathrm{d}[\ln w(\tau)] = Ł(\boldsymbol{q}, \tau)\,\mathrm{d}\tau \\ \Longrightarrow\quad & w(\tau_k + \Delta\tau_k) \approx w(\tau_k)\,\mathrm{e}^{Ł(\boldsymbol{Q}(\tau_k), \tau_k)\,\Delta\tau_k}. \end{aligned} \tag{18}$$

Note that the weight remains unchanged if $Ł = 0$. Sources can also be included in Eq. 15 and incorporated into the SDE formulation (see e.g. Kopp et al. 2012; Strauss & Effenberger 2017), but this is unnecessary here. Although SDEs are unconditionally stable (with bounded stochastic drift and diffusion coefficients, so that an initial error would not grow in the numerical scheme; see Kloeden & Platen 1995; Strauss & Effenberger 2017), one should still choose a sufficiently small time step to resolve physical structures or processes. To avoid time steps that are either too large or too small, which would yield inaccurate results or long execution times, respectively, one can use an adaptive time step that changes at each iteration to ensure sufficient sampling of the length scale l_i of q_i. This is generally written as (see Strauss & Effenberger 2017)

$$\Delta\tau_k(\boldsymbol{Q}(\tau_k), \tau_k) = \min\left\{ \frac{l_i(\boldsymbol{Q}(\tau_k), \tau_k)}{|a_i(\boldsymbol{Q}(\tau_k), \tau_k)|}; \frac{l_i^2(\boldsymbol{Q}(\tau_k), \tau_k)}{\sum_j \mathsf{B}_{ij}^2(\boldsymbol{Q}(\tau_k), \tau_k)} \right\}. \tag{19}$$

We implemented this numerical scheme in C and computed the pseudo-particles independently using Open MPI (Gabriel et al. 2004).

Pei et al. (2010), Kopp et al. (2012), and Strauss & Effenberger (2017) cover most aspects of the SDE solution for the Parker TPE, whereas Wijsen (2020) and van den Berg (2023) discuss aspects of solving the FTE using SDEs. For the current application, the phase-space coordinates with spherical spatial coordinates are $\boldsymbol{q} = [r, \theta, \phi, p, \mu]^\mathrm{T}$, and we indicate the random variables below by $\boldsymbol{Q} = [R, \Theta, \Phi, \Pi, M]^\mathrm{T}$. We give the exact forms of the SDEs in spherical spatial coordinates in Sects 3.2.1 and 3.2.2, with further mathematical details in Appendix A. We have generalised the following discussion to the FTE, including μ. Therefore, parts related to the pitch cosine do not apply to the Parker TPE. The reflective inner boundary condition implies that

$$R \leftarrow 2r_\odot - R \quad \text{and} \quad M \leftarrow |M| \quad \text{if} \quad R < r_\odot, \tag{20}$$

although this condition is only necessary numerically and in the Parker TPE, as magnetic mirroring should keep pseudo-particles away from this boundary in the FTE. We applied coordinate renormalisation to restrict θ, ϕ, and μ to $[0; \pi]$, $[0; 2\pi)$, and $[-1; 1]$, respectively. We did this by

$$\begin{cases} \Theta \leftarrow |\Theta| & \text{and} \quad \Phi \leftarrow \Phi + \pi \quad \text{if} \quad \Theta < 0 \\ \Theta \leftarrow 2\pi - \Theta & \text{and} \quad \Phi \leftarrow \Phi - \pi \quad \text{if} \quad \Theta > \pi \end{cases}, \tag{21}$$

[5] `https://www.pcg-random.org/`

followed by

$$\begin{cases} \Phi \leftarrow \Phi + 2\pi & \text{if} \quad \Phi < 0 \\ \Phi \leftarrow \Phi - 2\pi & \text{if} \quad \Phi \geq 2\pi \end{cases}, \tag{22}$$

together with

$$M \leftarrow \operatorname{sign}(M)\, 2 - M \quad \text{if} \quad |M| > 1, \tag{23}$$

where the re-normalisation of Θ and M follows a reflecting boundary condition, while that of Φ follows a periodic boundary condition (Kopp et al. 2012; Strauss & Effenberger 2017; van den Berg 2023). The adaptive time step is

$$\Delta\tau = \tag{24}$$
$$\min\left\{\frac{l_r}{|a_r|}; \frac{l_\theta}{|a_\theta|}; \frac{l_\phi}{|a_\phi|}; \frac{l_p}{|a_p|}; \frac{l_\mu}{|a_\mu|}; \frac{l_r^2}{\mathsf{B}_{rr}^2 + \mathsf{B}_{r\phi}^2}; \frac{l_\theta^2}{\mathsf{B}_{\theta\theta}^2}; \frac{l_\phi^2}{\mathsf{B}_{\phi\phi}^2}; \frac{l_\mu^2}{\mathsf{B}_{\mu\mu}^2}\right\}.$$

We discuss the components of $\boldsymbol{a}$ and the elements of B below, separately for the Parker and focused TPEs. Following van den Berg (2023), we mainly related the length scales to the MFPs and the focusing length by a small fraction $\ell = 2^{-6}$, i.e.

$$\begin{aligned} l_r &= \ell \min\{L_r; \lambda_{rr}\} \\ &= \ell \min\left\{L\cos\psi; 3\,\frac{\kappa_\parallel \cos^2\psi + \kappa_{\perp r}\sin^2\psi}{v}\right\}, \end{aligned} \tag{25a}$$

$$l_\theta = \frac{\ell\lambda_{\theta\theta}}{r} = \frac{3\ell\kappa_{\perp\theta}}{vr}, \tag{25b}$$

$$\begin{aligned} l_\phi &= \frac{\ell}{r\sin\theta}\min\{L_\phi; \lambda_{\phi\phi}\} \\ &= \frac{\ell}{r\sin\theta}\min\left\{L\sin\psi; 3\,\frac{\kappa_\parallel \sin^2\psi + \kappa_{\perp r}\cos^2\psi}{v}\right\}, \end{aligned} \tag{25c}$$

$$l_p = \ell p, \tag{25d}$$

$$l_\mu = \ell\sqrt{1-\mu^2}. \tag{25e}$$

In the time-backward approach, all pseudo-particles start at the observation point, say $(R(0), \Theta(0), \Phi(0)) = (r_\mathrm{f}, \theta_\mathrm{f}, \phi_\mathrm{f}) = (r_\oplus, \pi/2, 0)$ as an example for Earth, with some kinetic energy K_f (corresponding to momentum $\Pi(0) = p_\mathrm{f}$), pitch cosine $M(0) = \mu_\mathrm{f}$ (uniformly distributed on $[-1; 1]$), and weight $w(0) = w_\mathrm{f} = 1$. They are traced backwards in time until they reach the outer boundary at time τ_b, with weights $w(\tau_\mathrm{b}) = w_\mathrm{b}$ and energies $K_\mathrm{b} \geq K_\mathrm{f}$ (corresponding to momentum $\Pi(\tau_\mathrm{b}) = p_\mathrm{b}$, assuming no acceleration in the heliosphere so that particles lose energy as they propagate from the outer boundary to the observer in the physical, time-forward approach). The spectrum at the observation point at energy K_f is the weighted average over all pseudo-particles of Eq. 5, evaluated with their K_b (see Strauss & Effenberger 2017). Explicitly,

$$\hat{\jmath}_K(r_\mathrm{f}, \theta_\mathrm{f}, K_\mathrm{f}) = \frac{p_\mathrm{f}^2}{W}\sum_l \frac{w_{\mathrm{b}l}\, j_\mathrm{o}(K_{\mathrm{b}l})}{p_{\mathrm{b}l}^2}, \tag{26}$$

where the summation is over all pseudo-particles injected with K_f, regardless of their pitch angles (this is consistent with the assumption of pitch-angle isotropy at the outer boundary), $W = \sum_l w_{\mathrm{b}l}$ is the sum of all the weights, and the ratio of momenta follows from the conversion between differential and omnidirectional intensities (note that the hat indicates that this is a discrete estimate of the continuous function it represents). We used the weighted standard deviation of the (assumed) independent and identically distributed random variables that comprise this weighted mean as an indication of its uncertainty, i.e.

$$\delta\hat{\jmath}_K \approx \frac{1}{W}\sqrt{\left[\frac{p_\mathrm{f}^4}{W}\sum_l \frac{w_{\mathrm{b}l}\, j_\mathrm{o}^2(K_{\mathrm{b}l})}{p_{\mathrm{b}l}^4} - \hat{\jmath}_K^2\right]\sum_l w_{\mathrm{b}l}^2}. \tag{27}$$

Although we started the pseudo-particles isotropically at the observer, each pseudo-particle contributes a different weight, potentially resulting in an anisotropic distribution at the observer. Also note from Sect. 3.1 and the rest of this section that none of the coefficients or calculations depend on ϕ. Hence, if one constructs the solution only as a function of (r, θ, K, μ), the evolution of Φ can be neglected, thereby reducing the number of SDEs by one. We used 90 radial, 22 latitudinal, 30 kinetic-energy, and 20 pitch-cosine bins. When solving the Parker TPE, we used 150 pseudo-particles per radial, latitudinal, and energy bin, whereas we used 300 pseudo-particles per bin when solving the FTE. More particles are needed to reduce statistical noise and resolve the pitch-angle distribution (PAD). Initial estimates indicate that at least five times as many pseudo-particles are needed to calculate the anisotropy, and even more would be needed to resolve the PAD. However, computing the solution across the entire heliosphere using the FTE is computationally expensive, as it requires resolving fast pitch-angle scattering. To remedy this, we applied a three-point average across latitude, radius, and kinetic energy (in that order) to smooth the results. We discuss the testing and verification of this newly developed SDE model in Appendix B.

3.2.1. Stochastic Parker model

The Parker TPE (Eq. 4) can be written compactly in the form of Eq. 15, i.e.

$$-\frac{\partial F_0}{\partial\tau} = (\nabla\cdot\kappa - \boldsymbol{u})\cdot\nabla F_0 + \frac{p\,(\nabla\cdot\boldsymbol{u})}{3}\frac{\partial F_0}{\partial p} + \frac{2\,\kappa : \nabla\nabla F_0}{2}, \tag{28}$$

with $\boldsymbol{V}_\mathrm{d}$ neglected since we did not use it here, but this expression becomes lengthy in spherical coordinates (see Kopp et al. 2012). For the Parker HMF, the isotropic diffusion tensor,

$$\begin{aligned} \kappa &= \begin{bmatrix} \kappa_{rr} & \kappa_{r\theta} & \kappa_{r\phi} \\ \kappa_{\theta r} & \kappa_{\theta\theta} & \kappa_{\theta\phi} \\ \kappa_{\phi r} & \kappa_{\phi\theta} & \kappa_{\phi\phi} \end{bmatrix} \\ &= \begin{bmatrix} \kappa_\parallel\cos^2\psi + \kappa_{\perp r}\sin^2\psi & 0 & (\kappa_{\perp r} - \kappa_\parallel)\sin\psi\cos\psi \\ 0 & \kappa_{\perp\theta} & 0 \\ (\kappa_{\perp r} - \kappa_\parallel)\sin\psi\cos\psi & 0 & \kappa_\parallel\sin^2\psi + \kappa_{\perp r}\cos^2\psi \end{bmatrix}, \end{aligned} \tag{29}$$

is symmetric in spherical coordinates (Vos 2011; Potgieter 2013; Raath 2015). With the heliosphere setup described in Sect. 3.1, Eq. 28 simplifies in spherical coordinates to

$$\begin{aligned} -\frac{\partial F_0}{\partial\tau} = {} & \frac{p}{3}\left(\frac{2u_r}{r} + \frac{\partial u_r}{\partial r}\right)\frac{\partial F_0}{\partial p} + \frac{1}{r^2}\left(\kappa_{\theta\theta}\cot\theta + \frac{\partial\kappa_{\theta\theta}}{\partial\theta}\right)\frac{\partial F_0}{\partial\theta} + {} \\ & \left[\frac{1}{r}\left(2\kappa_{rr} + \csc\theta\,\frac{\partial\kappa_{\phi r}}{\partial\phi}\right) + \frac{\partial\kappa_{rr}}{\partial r} - u_r\right]\frac{\partial F_0}{\partial r} + {} \\ & \frac{\csc\theta}{r^2}\left[\kappa_{r\phi} + \csc\theta\,\frac{\partial\kappa_{\phi\phi}}{\partial\phi} + r\left(\frac{\partial\kappa_{r\phi}}{\partial r} - u_\phi\right)\right]\frac{\partial F_0}{\partial\phi} + {} \\ & \frac{1}{2}\left[2\kappa_{rr}\frac{\partial^2 F_0}{\partial r^2} + \frac{2\kappa_{\theta\theta}}{r^2}\frac{\partial^2 F_0}{\partial\theta^2} + \frac{2\kappa_{\phi\phi}}{r^2\sin^2\theta}\frac{\partial^2 F_0}{\partial\phi^2} + {}\right. \\ & \left.\frac{2(\kappa_{r\phi} + \kappa_{\phi r})}{r\sin\theta}\frac{\partial^2 F_0}{\partial r\,\partial\phi}\right]. \end{aligned} \tag{30}$$

One can easily identify the SDEs from the latter expression, i.e.

$$a_r = \frac{1}{r}\left(2\kappa_{rr} + \csc\theta\,\frac{\partial\kappa_{\phi r}}{\partial\phi}\right) + \frac{\partial\kappa_{rr}}{\partial r} - v_{\rm sw}, \tag{31a}$$

$$a_\theta = \frac{1}{r^2}\left(\kappa_{\theta\theta}\cot\theta + \frac{\partial\kappa_{\theta\theta}}{\partial\theta}\right), \tag{31b}$$

$$a_\phi = \frac{\csc\theta}{r^2}\left[\kappa_{r\phi} + \csc\theta\,\frac{\partial\kappa_{\phi\phi}}{\partial\phi} + r\left(v_{\rm sw}\tan\psi + \frac{\partial\kappa_{r\phi}}{\partial r}\right)\right], \tag{31c}$$

$$a_p = \frac{p}{3}\left(\frac{2v_{\rm sw}}{r} + \frac{\partial v_{\rm sw}}{\partial r}\right), \tag{31d}$$

where we substituted Eq. 6, $2v_{\rm sw}/r + \partial v_{\rm sw}/\partial r$ is the total divergence of an accelerating SW (Eq. A.7b), and

$$\mathsf{C} = \begin{bmatrix} \mathsf{C}_{rr} & 0 & \mathsf{C}_{r\phi} \\ 0 & \mathsf{C}_{\theta\theta} & 0 \\ \mathsf{C}_{\phi r} & 0 & \mathsf{C}_{\phi\phi} \end{bmatrix} = 2\begin{bmatrix} \kappa_{rr} & 0 & \kappa_{r\phi}/r\sin\theta \\ 0 & \kappa_{\theta\theta}/r^2 & 0 \\ \kappa_{r\phi}/r\sin\theta & 0 & \kappa_{\phi\phi}/r^2\sin^2\theta \end{bmatrix} \tag{32}$$

is positive definite as long as $r \neq 0$ and $\theta \neq 0°$ or $\theta \neq 180°$. Note that we present only the spatial components of the diffusion tensors here because momentum diffusion is absent. Since we specified the SW only from the solar surface, the pseudo-particles will not reach $r = 0$ if we impose a boundary condition at $r_\odot$. By choosing B as an upper triangular matrix, it follows that (Pei et al. 2010; Kopp et al. 2012)

$$\mathsf{B} = \begin{bmatrix} \mathsf{B}_{rr} & \mathsf{B}_{r\theta} & \mathsf{B}_{r\phi} \\ 0 & \mathsf{B}_{\theta\theta} & \mathsf{B}_{\theta\phi} \\ 0 & 0 & \mathsf{B}_{\phi\phi} \end{bmatrix} = \begin{bmatrix} \sqrt{\mathsf{C}_{rr} - \mathsf{C}_{r\phi}^2/\mathsf{C}_{\phi\phi}} & 0 & \mathsf{C}_{r\phi}/\sqrt{\mathsf{C}_{\phi\phi}} \\ 0 & \sqrt{\mathsf{C}_{\theta\theta}} & 0 \\ 0 & 0 & \sqrt{\mathsf{C}_{\phi\phi}} \end{bmatrix} = \begin{bmatrix} \sqrt{2(\kappa_{rr} - \kappa_{r\phi}^2/\kappa_{\phi\phi})} & 0 & \kappa_{r\phi}\sqrt{2/\kappa_{\phi\phi}} \\ 0 & \sqrt{2\kappa_{\theta\theta}}/r & 0 \\ 0 & 0 & \sqrt{2\kappa_{\phi\phi}}/r\sin\theta \end{bmatrix}, \tag{33}$$

where $\kappa_{rr} \geq \kappa_{r\phi}^2/\kappa_{\phi\phi}$ must hold (and it should as long as $\kappa_{\perp r} \leq \kappa_{||}$). Alternatively, a lower-triangular matrix can be used, while an upper-triangular matrix, but with $\mathsf{B}_{r\theta} = 0$ and $\mathsf{B}_{\theta r} \neq 0$ (see Kopp et al. 2012), yields a similar matrix and the same condition for the Parker HMF used here. Another alternative given by Pei et al. (2010) yields a much more complex form. These alternatives might help keep B real in the exceptional case when $\kappa_{rr} < \kappa_{r\phi}^2/\kappa_{\phi\phi}$ (it is theoretically not expected that $\kappa_{\perp r} > \kappa_{||}$, and in the extreme case of isotropic turbulence, $\kappa_{\perp r} = \kappa_{||}$, so that $\kappa_{r\phi} = 0$), but they do not resolve the coordinate singularity at the poles in spherical coordinates. To avoid division by zero, we set the problematic terms to zero at the poles. However, if the time step is sufficiently small, physical processes should keep pseudo-particles away from the poles.

3.2.2. Stochastic focused model

The FTE (Eq. 1) in the form of Eq. 15 reads as

$$-\frac{\partial f}{\partial\tau} = (\boldsymbol{\nabla}\cdot\mathsf{D}_\perp - \boldsymbol{v}_{\rm gc})\cdot\boldsymbol{\nabla}f - \frac{{\rm d}p}{{\rm d}t}\frac{\partial f}{\partial p} + \left(\frac{\partial D_{\mu\mu}}{\partial\mu} - \frac{{\rm d}\mu}{{\rm d}t}\right)\frac{\partial f}{\partial\mu} + D_{\mu\mu}\frac{\partial^2 f}{\partial\mu^2} + \mathsf{D}_\perp : \boldsymbol{\nabla\nabla}f - \left(\boldsymbol{\nabla}\cdot\boldsymbol{v}_{\rm gc} + \frac{2}{p}\frac{{\rm d}p}{{\rm d}t} + \frac{\partial}{\partial p}\left[\frac{{\rm d}p}{{\rm d}t}\right] + \frac{\partial}{\partial\mu}\left[\frac{{\rm d}\mu}{{\rm d}t}\right]\right)f, \tag{34}$$

with the perpendicular diffusion tensor in spherical coordinates (Strauss & Fichtner 2015; van den Berg 2023),

$$\mathsf{D}_\perp = \begin{bmatrix} \mathsf{D}^\perp_{rr} & \mathsf{D}^\perp_{r\theta} & \mathsf{D}^\perp_{r\phi} \\ \mathsf{D}^\perp_{\theta r} & \mathsf{D}^\perp_{\theta\theta} & \mathsf{D}^\perp_{\theta\phi} \\ \mathsf{D}^\perp_{\phi r} & \mathsf{D}^\perp_{\phi\theta} & \mathsf{D}^\perp_{\phi\phi} \end{bmatrix} = \begin{bmatrix} D_{\perp r}(\mu)\sin^2\psi & 0 & D_{\perp r}(\mu)\sin\psi\cos\psi \\ 0 & D_{\perp\theta}(\mu) & 0 \\ D_{\perp r}(\mu)\sin\psi\cos\psi & 0 & D_{\perp r}(\mu)\cos^2\psi \end{bmatrix}, \tag{35}$$

being symmetric. Using the heliospheric setup of Sect. 3.1 and ${\rm d}v/{\rm d}p = {\rm d}\left[pc^2/\sqrt{p^2c^2 + E_0^2}\right]/{\rm d}p = v(1 - v^2/c^2)/p$ for the simplification of the linear term, with E_0 as the particle rest mass energy, Eq. 34 in spherical coordinates becomes

$$\begin{aligned} -\frac{\partial f}{\partial\tau} = &-\left\{\frac{\mu v}{c^2}\,\hat{b}\cdot\left[\frac{\partial\boldsymbol{u}}{\partial t} + (\boldsymbol{u}\cdot\boldsymbol{\nabla})\,\boldsymbol{u}\right]\right\}f + \\ &\left(-\frac{{\rm d}p}{{\rm d}t}\right)\frac{\partial f}{\partial p} + \left(\frac{\partial D_{\mu\mu}}{\partial\mu} - \frac{{\rm d}\mu}{{\rm d}t}\right)\frac{\partial f}{\partial\mu} + \\ &\left[\frac{1}{r}\left(2\mathsf{D}^\perp_{rr} + \csc\theta\,\frac{\partial\mathsf{D}^\perp_{\phi r}}{\partial\phi}\right) + \frac{\partial\mathsf{D}^\perp_{rr}}{\partial r} - \mu v b_r - u_r\right]\frac{\partial f}{\partial r} + \\ &\frac{1}{r^2}\left(\mathsf{D}^\perp_{\theta\theta}\cot\theta + \frac{\partial\mathsf{D}^\perp_{\theta\theta}}{\partial\theta}\right)\frac{\partial f}{\partial\theta} + \\ &\frac{\csc\theta}{r^2}\left[\mathsf{D}^\perp_{r\phi} + \csc\theta\,\frac{\partial\mathsf{D}^\perp_{\phi\phi}}{\partial\phi} + r\left(\frac{\partial\mathsf{D}^\perp_{r\phi}}{\partial r} - \mu v b_\phi - u_\phi\right)\right]\frac{\partial f}{\partial\phi} + \\ &\frac{1}{2}\left[2D_{\mu\mu}\frac{\partial^2 f}{\partial\mu^2} + 2\mathsf{D}^\perp_{rr}\frac{\partial^2 f}{\partial r^2} + \frac{2\mathsf{D}^\perp_{\theta\theta}}{r^2}\frac{\partial^2 f}{\partial\theta^2} + \right. \\ &\left.\frac{2\mathsf{D}^\perp_{\phi\phi}}{r^2\sin^2\theta}\frac{\partial^2 f}{\partial\phi^2} + \frac{2(\mathsf{D}^\perp_{r\phi} + \mathsf{D}^\perp_{\phi r})}{r\sin\theta}\frac{\partial^2 f}{\partial r\,\partial\phi}\right], \end{aligned} \tag{36}$$

where we neglected $\boldsymbol{v}_{\rm d}(\mu)$ again and did not explicitly write the linear term, ${\rm d}p/{\rm d}t$, and ${\rm d}\mu/{\rm d}t$ in spherical coordinates due to their complicated forms (see Appendix A for these terms in spherical coordinates).

Identifying the SDEs from the latter equation yielded

$$\text{Ł} = -\frac{\mu v}{c^2}\,\hat{b}\cdot\left[\frac{\partial\boldsymbol{u}}{\partial t} + (\boldsymbol{u}\cdot\boldsymbol{\nabla})\,\boldsymbol{u}\right] \tag{37}$$

for the linear coefficient and

$$a_r = \frac{1}{r}\left(2\mathsf{D}^{\perp}_{rr} + \csc\theta\,\frac{\partial \mathsf{D}^{\perp}_{\phi r}}{\partial\phi}\right) + \frac{\partial \mathsf{D}^{\perp}_{rr}}{\partial r} - \mu v\cos\psi - v_{\mathrm{sw}}, \tag{38a}$$

$$a_\theta = \frac{1}{r^2}\left(\mathsf{D}^{\perp}_{\theta\theta}\cot\theta + \frac{\partial \mathsf{D}^{\perp}_{\theta\theta}}{\partial\theta}\right), \tag{38b}$$

$$a_\phi = \frac{\csc\theta}{r^2}\left[\mathsf{D}^{\perp}_{r\phi} + \csc\theta\,\frac{\partial \mathsf{D}^{\perp}_{\phi\phi}}{\partial\phi} + r\left(\mu v\sin\psi + v_{\mathrm{sw}}\tan\psi + \frac{\partial \mathsf{D}^{\perp}_{r\phi}}{\partial r}\right)\right], \tag{38c}$$

$$a_p = -\frac{\mathrm{d}p}{\mathrm{d}t}, \tag{38d}$$

$$a_\mu = \frac{\partial D_{\mu\mu}}{\partial\mu} - \frac{\mathrm{d}\mu}{\mathrm{d}t} \tag{38e}$$

for the stochastic drift coefficients, with $\boldsymbol{u}$ (Eq. 6) and $\boldsymbol{b}$ (Eq. A.2) substituted. The perpendicular diffusion tensor,

$$\mathsf{C}_\perp = \begin{bmatrix} \mathsf{C}^{\perp}_{rr} & 0 & \mathsf{C}^{\perp}_{r\phi} \\ 0 & \mathsf{C}^{\perp}_{\theta\theta} & 0 \\ \mathsf{C}^{\perp}_{\phi r} & 0 & \mathsf{C}^{\perp}_{\phi\phi} \end{bmatrix} = 2\begin{bmatrix} \mathsf{D}^{\perp}_{rr} & 0 & \mathsf{D}^{\perp}_{r\phi}/r\sin\theta \\ 0 & \mathsf{D}^{\perp}_{\theta\theta}/r^2 & 0 \\ \mathsf{D}^{\perp}_{r\phi}/r\sin\theta & 0 & \mathsf{D}^{\perp}_{\phi\phi}/r^2\sin^2\theta \end{bmatrix}, \tag{39}$$

is positive definite as long as $r \neq 0$ and $\theta \neq 0°$ or $\theta \neq 180°$. For pitch-angle scattering, $\mathsf{B}_{\mu\mu} = \sqrt{2D_{\mu\mu}}$, and

$$\begin{aligned}\mathsf{B}_\perp &= \begin{bmatrix} \mathsf{B}^{\perp}_{rr} & \mathsf{B}^{\perp}_{r\theta} & \mathsf{B}^{\perp}_{r\phi} \\ 0 & \mathsf{B}^{\perp}_{\theta\theta} & \mathsf{B}^{\perp}_{\theta\phi} \\ 0 & 0 & \mathsf{B}^{\perp}_{\phi\phi} \end{bmatrix} = \begin{bmatrix} \sqrt{\mathsf{C}_{rr} - \mathsf{C}^2_{r\phi}/\mathsf{C}_{\phi\phi}} & 0 & \mathsf{C}_{r\phi}/\sqrt{\mathsf{C}_{\phi\phi}} \\ 0 & \sqrt{\mathsf{C}_{\theta\theta}} & 0 \\ 0 & 0 & \sqrt{\mathsf{C}_{\phi\phi}} \end{bmatrix} \\ &= \begin{bmatrix} \sqrt{2\left[\mathsf{D}^{\perp}_{rr} - (\mathsf{D}^{\perp}_{r\phi})^2/\mathsf{D}^{\perp}_{\phi\phi}\right]} & 0 & \mathsf{D}^{\perp}_{r\phi}\sqrt{2/\mathsf{D}^{\perp}_{\phi\phi}} \\ 0 & \sqrt{2\mathsf{D}^{\perp}_{\theta\theta}}/r & 0 \\ 0 & 0 & \sqrt{2\mathsf{D}^{\perp}_{\phi\phi}}/r\sin\theta \end{bmatrix} \\ &= \begin{bmatrix} 0 & 0 & \sqrt{2D_{\perp r}(\mu)}\,\sin\psi \\ 0 & \sqrt{2D_{\perp\theta}(\mu)}\,r^{-1} & 0 \\ 0 & 0 & \sqrt{2D_{\perp r}(\mu)}\,r^{-1}\csc\theta\cos\psi \end{bmatrix}\end{aligned} \tag{40}$$

for the spatial part of B chosen as an upper triangular matrix, where the condition $\mathsf{D}^{\perp}_{rr} \geq (\mathsf{D}^{\perp}_{r\phi})^2/\mathsf{D}^{\perp}_{\phi\phi}$ is not necessary in the FTE for the Parker HMF since $(\mathsf{D}^{\perp}_{r\phi})^2/\mathsf{D}^{\perp}_{\phi\phi} = D^2_{\perp r}(\mu)\sin^2\psi\cos^2\psi/D_{\perp r}(\mu)\cos^2\psi = D_{\perp r}(\mu)\sin^2\psi = \mathsf{D}^{\perp}_{rr}$ (van den Berg 2023). Note that the $v_{\mathrm{sw}}\tan\psi$ term in both Eqs 31c and 38c arises from solving the TPEs in the co-rotating frame (the only frame in which the Parker HMF form of Eq. 7 is valid), not from particles rigidly co-rotating with the Sun. However, this is inconsequential for GCRs in the steady state because we did not include the evolution of Φ in the SDEs, as described in the last paragraph of Sect. 3.2 (one only needs to account for it when transforming the solution into a stationary observer's frame).

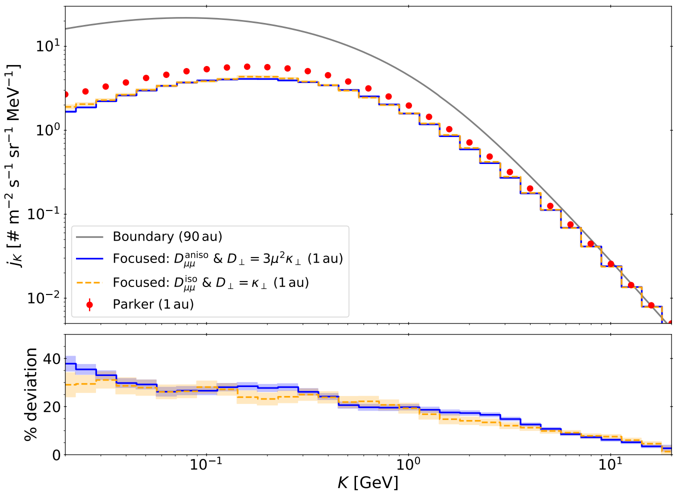

Fig. 2: Top: Proton spectrum at a radial distance of 1 au in the equatorial plane as a function of kinetic energy resulting from the Parker (red dots) and focused (steps) TPEs. Dashed orange and solid blue steps indicate the results from the FTE for isotropic pitch-angle scattering with pitch-angle-independent perpendicular diffusion and for anisotropic pitch-angle scattering with pitch-angle-dependent perpendicular diffusion, respectively. The solid grey line shows the spectrum at the outer boundary for reference. Bottom: Percentage deviation $(100\,|1 - j_K^{\mathrm{Focus}}/j_K^{\mathrm{Parker}}|)$ between the results of the Parker and focused TPEs in the top panel. Shaded regions indicate uncertainties.

4. Results

The top panel of Fig. 2 shows the proton spectrum at a radial distance of 1 au in the equatorial plane, as predicted by the Parker and focused TPEs, after smoothing the results using a three-point average over latitude, radius, and kinetic energy (in that order). Note that the model does not include modulation within the heliosheath and at the termination shock. Therefore, one should not directly compare these spectra with observations, as the intensities are too high; however, the aim of this study is rather to compare the results computed using the two different TPEs than to compare them with spacecraft observations. Unfortunately, we cannot observe the adiabatic limit (where $j_K \propto K$; shown in Appendix B) here because the kinetic energies are too high. We chose this limited energy range purely due to numerical constraints (a smaller ℓ is required for the adaptive time step of Eq. 24 at higher energies, and execution time increases drastically at lower energies because one must resolve efficient pitch-angle scattering). The FTE predicts a similar spectrum whether one uses isotropic pitch-angle scattering (Eq. 12a) with pitch-angle-independent perpendicular diffusion (Eq. 14 with $h = 1$) or anisotropic pitch-angle scattering (Eq. 12b) with pitch-angle-dependent perpendicular diffusion (Eq. 14 with $h = 3\mu^2$). This is expected, as van den Berg (2023) finds that the interplay between pitch-angle scattering and perpendicular diffusion becomes noticeable only when $\kappa_\perp \sim \kappa_\parallel$, whereas $\kappa_{\perp r}/\kappa_\parallel = \chi = 0.02$ and $\kappa_{\perp\theta}/\kappa_\parallel = \chi\varsigma = 0.06$ at most over the poles in this work. Given the similarity of these results, unless stated otherwise, we discuss only anisotropic pitch-angle scattering with pitch-angle-dependent perpendicular diffusion, as this scenario is more realistic. Most importantly, the spectrum predicted by the Parker TPE is higher at low kinetic energies than the spectrum predicted by the FTE.

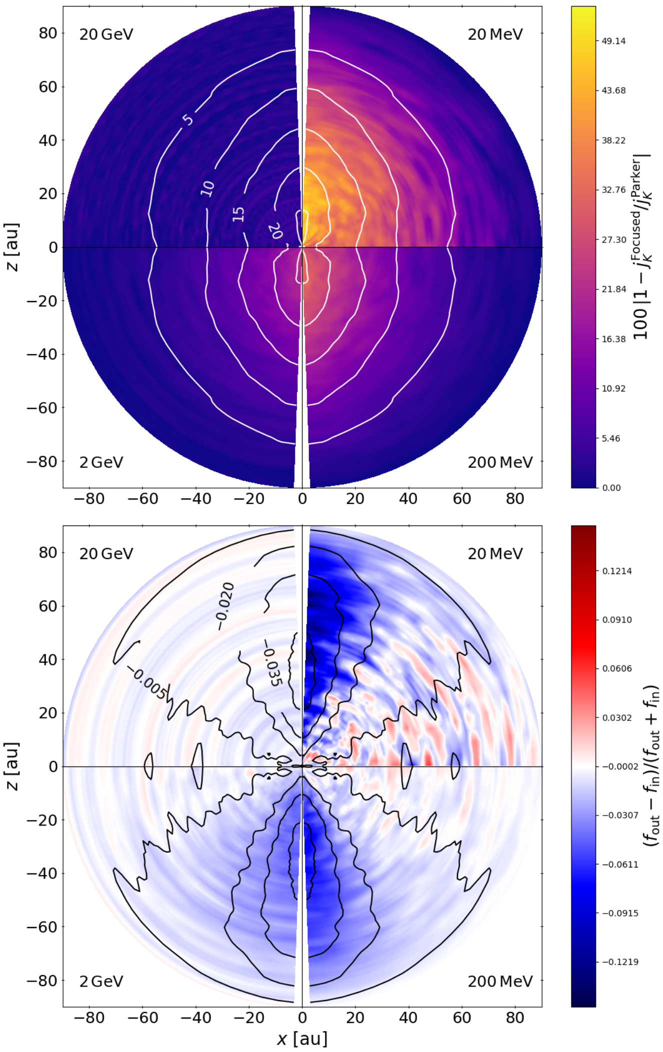

Fig. 3: Top: Percentage deviation between the results of the Parker TPE and the FTE with anisotropic pitch-angle scattering and pitch-angle-dependent perpendicular diffusion throughout the heliosphere for four energies (indicated in the quadrants) and averaged over all energies (contour lines). The equator and poles lie along the x- and z-axes, respectively. The innermost unlabelled contour line marks 25%. Bottom: Anisotropy proxy (Eq. 49) from the FTE with anisotropic pitch-angle scattering and pitch-angle-dependent perpendicular diffusion, presented in the same format as the top panel. The unlabelled contour line over the poles indicates a value of −0.05.

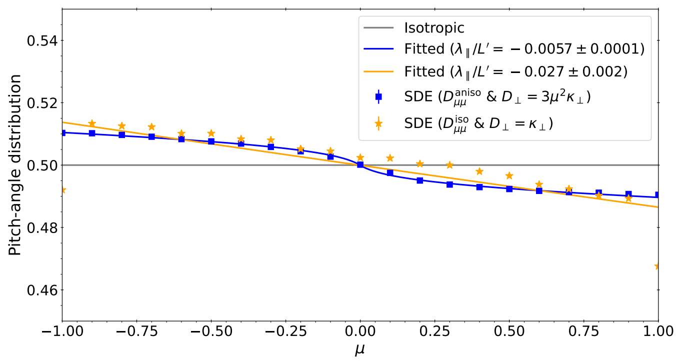

Fig. 4: Normalised PADs, averaged over all latitudes, radial distances, and kinetic energies (in that order), resulting from the FTE for isotropic pitch-angle scattering with pitch-angle-independent perpendicular diffusion (orange stars) and for anisotropic pitch-angle scattering with pitch-angle-dependent perpendicular diffusion (blue squares). The orange and blue lines indicate the analytical PADs from Eqs 47 and C.6, respectively, fitted to the simulations (with parameters shown in the legend). Negative pitch-cosine values indicate particles moving towards the Sun.

The bottom panel of Fig. 2 shows the percentage deviation between the results from the Parker and focused TPEs, indicating that the difference between the two TPEs increases as energy decreases. Below ∼ 200 MeV, the Parker TPE overestimates the intensity by ∼ 30%. The apparent ∼ 5% difference between the two FTE results at the lowest energies is an artefact of smoothing and does not reflect a physical difference (i.e. the unsmoothed results show no diverging trend within the uncertainties). To investigate the global behaviour of the Parker and focused TPEs, the top panel of Fig. 3 shows the percentage deviation between them across the heliosphere at four energies. Note that the model results are independent of longitude because of the spherical modulation cavity assumed here, and that the southern and northern hemispheres are mirror images of each other. At the highest energies, where the spectrum remains largely unmodulated, the difference between the Parker and focused TPEs is negligible. At the lowest energies, however, the difference increases towards the inner heliosphere and over the poles. Specifically, the percentage deviation over the poles reaches ∼ 40% at a radial distance of 1 au. This pattern develops gradually, shifting from high to low energies, and is also clearly visible in the percentage deviation averaged across all kinetic energies (as indicated by the contour lines, which we smoothed over radius and latitude).

To explain the difference between the Parker and focused TPEs, the initial quantities to examine were the first-order,

$$A_1 = \frac{3}{2F_0}\int_{-1}^{1} \mu f(\mu)\,\mathrm{d}\mu, \tag{41}$$

and second-order,

$$A_2 = \frac{5}{4F_0}\left[3\int_{-1}^{1} \mu^2 f(\mu)\,\mathrm{d}\mu - 2F_0\right], \tag{42}$$

anisotropies (see Beeck & Wibberenz 1986 and Lampa 2011 for their origins and formal definitions). The first-order anisotropy is proportional to the (distribution-weighted) average pitch cosine and indicates a preferred direction of motion along the magnetic field (van den Berg et al. 2020). The second-order anisotropy becomes significant when the first-order anisotropy is nearly zero and the distribution is not isotropic (i.e. when the distribution is an even function of the pitch cosine). Unfortunately, the statistical fluctuations inherent in SDEs are too large to discern any systematic behaviour in these anisotropy measurements. However, averaging the normalised PAD,

$$\tilde{f}(\mu) = \frac{f(\mu)}{\int_{-1}^{1} f(\eta)\,\mathrm{d}\eta} = \frac{f(\mu)}{2F_0}, \tag{43}$$

across regions of phase space revealed its general shape. Figure 4 shows the normalised PADs, averaged over the entire phase space and smoothed with a three-point average over pitch cosine, resulting from the FTE. For isotropic pitch-angle scattering with pitch-angle-independent perpendicular diffusion, the smaller values at $|\mu| = 1$, together with the overall noisiness of the PAD, suggest that the time step may have been too large. More particles are moving towards the Sun than away from it, as one might expect for GCRs diffusing into the heliosphere. Since the PADs are odd functions of the pitch cosine, it is expected that the second-order anisotropy is smaller than the first-order anisotropy.

The shape of the PAD in Fig. 4 depends on whether isotropic or anisotropic pitch-angle scattering occurs. The physical processes of pitch-angle transport should explain these shapes. Retaining only focusing and pitch-angle scattering in the steady-state solution of the FTE,

$$\frac{\mathrm{d}}{\mathrm{d}\mu}\left[\frac{(1-\mu^2)v}{2L'}\tilde{f}\right] = \frac{\mathrm{d}}{\mathrm{d}\mu}\left[D_{\mu\mu}\frac{\mathrm{d}\tilde{f}}{\mathrm{d}\mu}\right], \tag{44}$$

and integrating twice from -1 to μ yields

$$\tilde{f}(\mu) = \frac{\mathrm{e}^{G(\mu)}}{\int_{-1}^{1}\mathrm{e}^{G(\eta)}\,\mathrm{d}\eta}, \tag{45}$$

where

$$G(\mu) = \frac{v}{2L'}\int_{-1}^{\mu}\frac{1-\eta^2}{D_{\mu\mu}(\eta)}\,\mathrm{d}\eta. \tag{46}$$

Here, we used the fact that $D_{\mu\mu} \propto 1-\mu^2$ and applied a normalisation condition (i.e. $\int_{-1}^{1}\tilde{f}(\mu)\,\mathrm{d}\mu = 1$) to calculate the integration constant. This expression parameterises all the physical processes affecting the PAD as $L' D_{\mu\mu}$, and its effective value is therefore not the local value at the point of investigation (Beeck & Wibberenz 1986). Alternatively, neglecting the temporal evolution and phase-space coordinates implies that this PAD represents a stationary solution of the distribution, averaged over a part of phase space. For isotropic pitch-angle scattering (Eq. 12a), the PAD can be readily calculated, yielding

$$\tilde{f}_{\mathrm{iso}}(\mu) = \frac{\xi\,\mathrm{csch}\,\xi}{2}\,\mathrm{e}^{\xi\mu}, \tag{47}$$

where $\xi = \lambda_{\|}/L'$, with $G(\mu) = \xi(1+\mu)$ (van den Berg et al. 2020 defined $G(\mu)$ slightly differently but obtained the same PAD), from which the first-order anisotropy can be calculated to be

$$A_1^{\mathrm{iso}} = 3\left(\coth\xi - \frac{1}{\xi}\right). \tag{48}$$

Fitting this PAD to the isotropic pitch-angle scattering with pitch-angle-independent perpendicular diffusion results shown in Fig. 4 (excluding the two points at $|\mu| = 1$; orange line) yields $\xi = -(2.7 \pm 0.2) \times 10^{-2}$. The PAD can be approximated by a straight line for such a small parameter, although the fit appears less accurate due to noise in the PAD. The first-order anisotropy can be calculated from the fitted ξ, with negative ξ- and A_1-values indicating that more particles are moving towards the Sun than away from it. Remember that the PAD includes signatures of all physical processes, meaning that the fitted value of ξ is an 'effective' value and does not represent the local value of $\lambda_{\|}/L'$ at the point under consideration (i.e. compare this example with what might be expected from Fig. 1; also bear in mind that we consider the PAD averaged over large regions of phase space). The PAD and first-order anisotropy can also be derived for anisotropic pitch-angle scattering (Eq. 12b), but the derivation is more complex, and we present it only in Appendix C. For anisotropic pitch-angle scattering with pitch-angle-dependent perpendicular diffusion, fitting the PAD (Eq. C.6; blue line in Fig. 4) yields $\xi = -(5.7 \pm 0.1) \times 10^{-3}$. This smaller ξ-value, compared with that for isotropic pitch-angle scattering, despite both models sharing the same focusing length and parallel MFP, demonstrates that the fitted value is merely an effective estimate. The fact that the shapes of these PADs can be described by the analytical expectations derived from the PADC further confirms that the FTE model is functioning correctly.

By averaging the normalised PADs over only two of the three phase-space coordinates and fitting the analytical PADs, the anisotropies can be characterised as a function of a single coordinate. Figure 5 shows the average dependence of the first- and second-order anisotropies on kinetic energy, radial distance, and latitude (we smoothed the fitted parameter using a three-point average over kinetic energy or latitude and a five-point average over radial distance before calculating the anisotropies). The anisotropies derived from both isotropic and anisotropic pitch-angle scattering are similar, as expected given the comparable spectra of the two models. The second-order anisotropy arising from isotropic pitch-angle scattering is approximately twice as large, consistent with using different pitch-angle dependencies for the CFDC. The second-order anisotropy has a smaller magnitude than the first-order anisotropy, as expected given the odd functions of the PADs, and it is smaller when the magnitude of the first-order anisotropy is also smaller (such a small anisotropy is probably not measurable by particle detectors, but we discuss the second-order anisotropy here for its theoretical importance in explaining differences between the Parker and focused TPEs). The distributions are more anisotropic at low energies, between $\sim 20-40$ au, and over the poles.

To assess how anisotropy varies across the heliosphere, the bottom panel of Fig. 3 shows the quantity

$$\mathcal{R} = \frac{f_{\mathrm{out}} - f_{\mathrm{in}}}{f_{\mathrm{out}} + f_{\mathrm{in}}} = \frac{\int_0^1 f(\mu)\,\mathrm{d}\mu - \int_{-1}^0 f(\mu)\,\mathrm{d}\mu}{\int_{-1}^1 f(\mu)\,\mathrm{d}\mu}, \tag{49}$$

where $f_{\mathrm{out}} = \int_0^1 f(\mu)\,\mathrm{d}\mu$ and $f_{\mathrm{in}} = \int_{-1}^0 f(\mu)\,\mathrm{d}\mu$ represent the parts of the distribution of particles moving away and towards the Sun, respectively, as a proxy for anisotropy, presented in the same format as the percentage deviation in the top panel (we first integrated the original distribution function, then smoothed f_{out}, f_{in}, and $f_{\mathrm{out}} + f_{\mathrm{in}}$ separately over latitude, radius, and kinetic energy before calculating $\mathcal{R}$). van den Berg et al. (2020) originally introduced this quantity as the fraction of SEPs released at the Sun. Unfortunately, this quantity is not simply related to the first-order anisotropy (as discussed by van den Berg et al. 2020)[6], but it displays distinct spatial and energy dependencies. This is because partial integration over pitch cosine smooths the distribution somewhat, even though the distribution function remains too noisy to calculate the first-order anisotropy at each phase-space point. The streaky pattern of the anisotropy proxy in the bottom panel of Fig. 3 at high energies, compared with the patchy pattern at low energies, suggests that the time step may be too large at high energies. Nonetheless, the proxy indicates that the distribution is nearly isotropic at the highest energies. At lower energies, however, particles tend to move preferentially towards the Sun over the poles and away from the Sun in the equatorial region. When we average the anisotropy proxy over energy (and smooth it over radius and latitude), the distribution appears nearly isotropic in the equatorial region, though particles moving

[6] The anisotropy proxy would be one-third of the first-order anisotropy if the particles moved exactly along the magnetic field (i.e. if μ could only take values of ± 1).

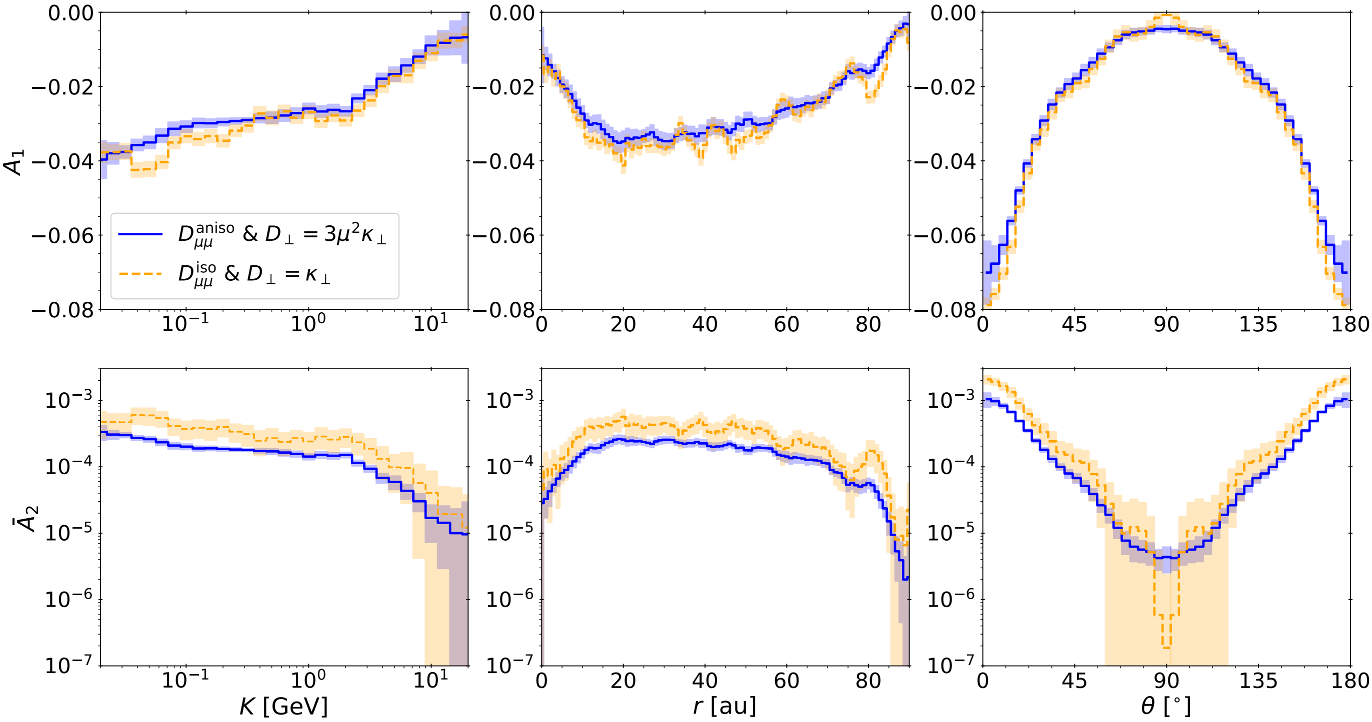

Fig. 5: First- (top) and second-order (bottom) anisotropies, calculated by fitting Eqs 47 (dashed orange) or C.6 (solid blue) to the simulated PADs, averaged over all latitudes and radial distances (left), latitudes and kinetic energies (middle), or radial distances and kinetic energies (right). We used Eqs 48 and C.10 to determine the first-order anisotropy, and we numerically integrated the fitted distributions using Eq. 42 to calculate the second-order anisotropy (for simplicity, especially in the case of anisotropic pitch-angle scattering).

towards the Sun over the poles remain visible (see the contour lines).

The anisotropy proxy patterns resemble the trends observed in the first-order anisotropy: both A_1 and $\mathcal{R}$ are predominantly negative throughout the heliosphere, with the largest values near the poles between $\sim 20-60$ au. This pattern is expected because the diffusion condition ($\lambda_\parallel < |L'|$) is satisfied in the equatorial region (compare the solid orange and grey lines in Fig. 1), but not over the poles (compare the dashed orange and grey lines in Fig. 1), where focusing becomes more significant relative to pitch-angle scattering (due to very large MFPs). The anisotropy patterns also resemble those of the percentage deviation, though not exactly: the difference between the Parker and focused TPE results is greater closer to the Sun, with a slight latitudinal dependence, whereas the anisotropy proxy shows a strong latitudinal dependence and peaks between $\sim 20-60$ au from the Sun. Naively, one might expect the largest anisotropy, and thus the greatest difference between the Parker and focused TPEs, to occur in the outer heliosphere where the parallel MFP is largest, but this does not account for transport processes. One could interpret this spatial mismatch as a sign of transport effects that lead to anisotropy causing a non-local difference between the Parker and focused TPEs at different locations. However, caution is needed, as this does not reflect the true anisotropy, and pitch-angle-weighted fluxes drive the differences between the TPEs (see the following discussions). Still, the anisotropic distribution could influence particle energy losses and spatial transport, potentially causing the Parker TPE to underestimate the modulation. The presence of a non-negligible anisotropy may explain the discrepancy between the Parker and focused TPEs and warrants further investigation.

To explain these specific anisotropy patterns, we considered the flux from the Parker TPE. Each spatial component of the flux, J_i, has an associated anisotropy amplitude of $3J_i/vF_0$ (see e.g. Jokipii & Parker 1970; Quenby 1984), implying that a non-zero flux must be associated with a non-zero anisotropy, and vice versa. For the model setup considered here, the following are the various spatial fluxes:

$$J_r = u_r F_0 - \kappa_{rr}\frac{\partial F_0}{\partial r}, \tag{50a}$$

$$J_\theta = -\frac{\kappa_{\theta\theta}}{r}\frac{\partial F_0}{\partial \theta}, \tag{50b}$$

where $u_r = v_{\rm sw}$ is the radial component of the flow velocity, $\kappa_{rr} = \kappa_\parallel \cos^2\psi + \kappa_{\perp r}\sin^2\psi$ is the radial DC, and $\kappa_{\theta\theta} = \kappa_{\perp\theta}$ is the polar DC (see Sect. 3.2.1; we did not consider the longitudinal flux here, since we assumed a spherical heliosphere with no longitudinal dependencies). The radial flux results from an outward advective flux and an inward diffusive flux, whereas the polar flux results solely from a diffusive flux directed from the poles towards the equator. Interestingly, these fluxes suggest that the advective anisotropy is $3v_{\rm sw}/v$, which is small for most high-energy particles, whereas the diffusive anisotropies are the product of a MFP per unit radius and the spatial power-law index of the omni-directional intensity, i.e. $-\lambda_{rr}(\partial \ln F_0/\partial r)$ or $-(\lambda_{\theta\theta}/r)(\partial \ln F_0/\partial\theta)$. Note that this flux anisotropy is not directly comparable to the usual first- or second-order anisotropy, nor to the anisotropy proxy of Eq. 49, because it is oriented along a specific spatial coordinate and is not defined relative to the HMF.

Figure 6 shows the various fluxes at four kinetic energies. The latitudinal dependence of the SW is evident in the radial ad-

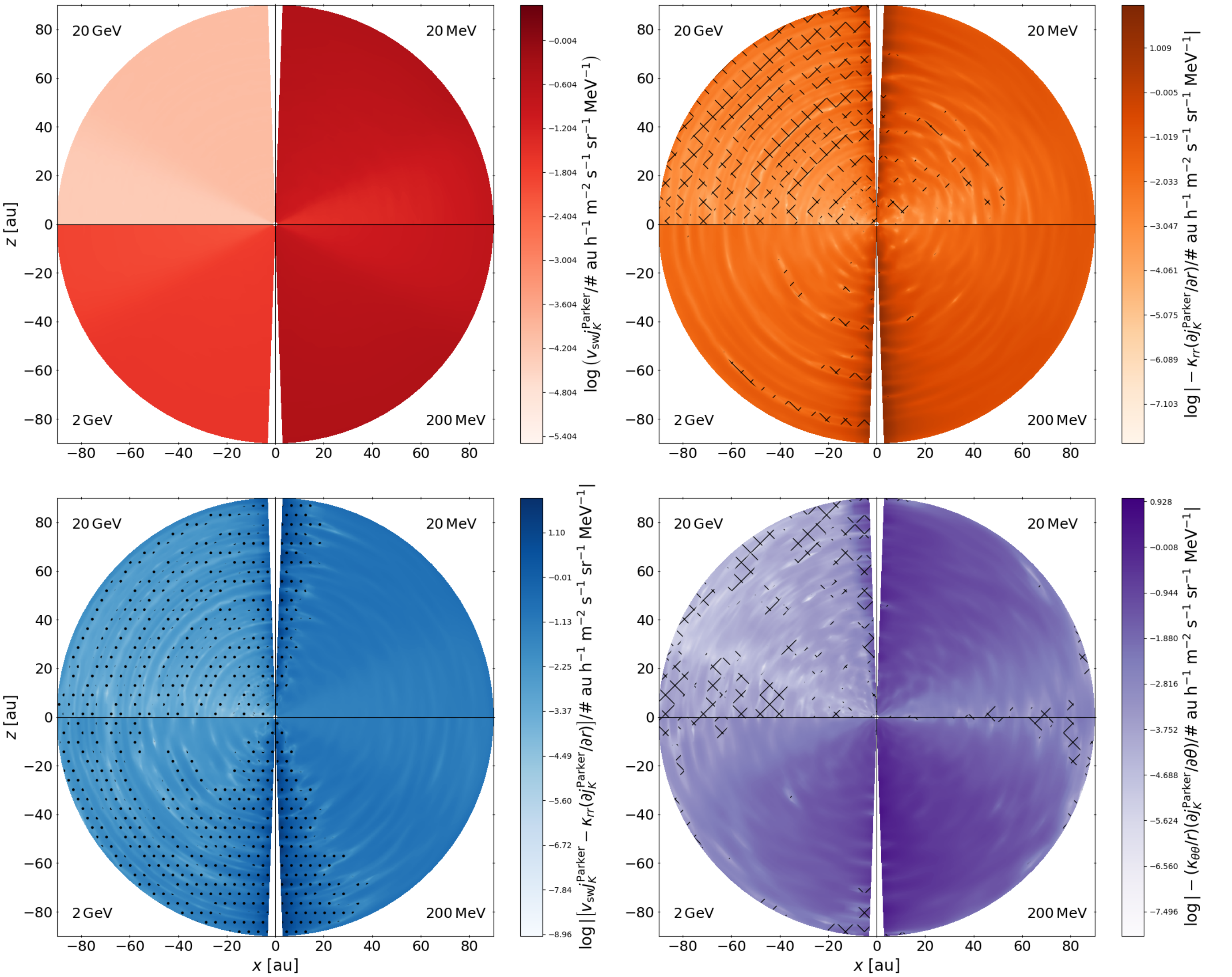

Fig. 6: Radial advective (top left), radial diffusive (top right), total radial (bottom left), and polar diffusive (bottom right) fluxes throughout the heliosphere, resulting from the Parker TPE, for different energies (indicated in the quadrants). Hatches in the right panels indicate flux directed opposite to what is expected, and dots in the bottom-left panel indicate inward flux.

vective flux (top-left panel). The numerical derivative of $\hat{j}_K$ is, unfortunately, noisy when calculating the diffusive flux (even after smoothing the derivative across latitude, radius, and kinetic energy). The diffusive flux directed opposite to what is expected, especially at the highest energies, appears to arise from numerical derivatives, as there is no physical mechanism in the model that could produce it (although this is unclear in the figure, the radial diffusive flux alternates between inward and outward). Therefore, the behaviour of both the radial and polar diffusive fluxes (right panels) is unclear at the highest energies due to numerical noise. However, at lower energies, the radial diffusive flux (top-right panel) is clearly greater over the poles than in the equatorial region. The polar diffusive flux (bottom-right panel) is also larger over the poles than in the equatorial region and displays the latitudinal dependence of the CFDC. The polar diffusive flux is generally smaller in magnitude than the radial diffusive flux because it reflects only the slower perpendicular diffusion. Nevertheless, at low energies, the polar diffusive flux is significantly higher than at high energies over the poles, indicating that perpendicular diffusion efficiently transports low-energy particles from the poles to the equator. The total radial flux (bottom-left panel) exhibits a more complex structure: the inward (marked by dots) diffusive flux dominates the outward advective flux at high energies (note that the dots at the highest energies do not contradict the outward diffusive flux marked by the hatched areas, as the flux alternates direction due to numerical noise); however, at progressively lower energies, the outward advective flux begins to dominate the inward diffusive flux, except over the poles. This is caused by a combination of smaller MFPs for lower-energy particles and a radial diffusive flux dominated by large parallel MFPs over the poles and small perpendicular MFPs in the equatorial region (see the black dash-dotted line in Fig. 1). SW advection (parallel diffusion) explains the outward- (inward-) moving particles observed in the anisotropy proxy in Fig. 3 at low energies in the equatorial region (over the poles).

5. Discussion

The previous section covered the results that could be obtained realistically and reliably from the SDE simulations. However, further discussion is needed to provide a more physical interpretation and summary of these results. Unfortunately, the fluxes in Eq. 50 do not account for energy losses and can be considered 'local spatial' fluxes. In reality, it is unlikely that a 20 MeV particle diffused from the outer boundary into the inner heliosphere. Instead, a higher-energy particle would lose energy as it diffused against the outward-directed SW, experiencing varying diffusion and energy-loss conditions along the way. To account for energy losses, Parker (1967) calculated the flux using the radial component of the Parker TPE (Eq. B.1; see also the discussion in Jokipii & Parker 1970). The radial part of the stationary solution of Eq. 4 can be written as

$$\frac{1}{r^2}\frac{\partial}{\partial r}\left[r^2 J_r\right] = \frac{1}{p^2}\frac{\partial}{\partial p}\left[\frac{p^3}{3r^2}\frac{\partial}{\partial r}\left(r^2 u_r\right)F_0\right], \tag{51}$$

and integration over radial distance yields

$$J_r(r,p) = \frac{1}{3r^2p^2}\frac{\partial}{\partial p}\left[p^3\int_0^r r'\left(2u_r + r'\frac{\partial u_r}{\partial r'}\right)F_0\,\mathrm{d}r'\right], \tag{52}$$

keeping in mind that $u_r = v_{\mathrm{sw}}(r,\theta)$ and $F_0(r,\theta,p)$. However, this form of the radial flux is valid only for a spherically symmetric heliosphere and assumes that $\kappa_\perp = \kappa_\parallel$, $\boldsymbol{V}_\mathrm{d} = \mathbf{0}$, and that there are no latitudinal dependencies in the DC or SW speed (see Appendix B). Nonetheless, if we perform this calculation for each radial spoke at different latitudes (not shown), the latitudinal dependence of the SW becomes evident in the flux due to energy losses arising from its divergence. Furthermore, the flux is negative (i.e. directed towards the Sun) at high energies and positive (i.e. directed away from the Sun) at low energies. This behaviour arises from energy losses proportional to $\partial F_0/\partial p$, with the shape of the spectrum yielding $\partial F_0/\partial p > 0$ ($\partial F_0/\partial p < 0$) at low (high) energies. Therefore, this approach does not account for the diffusive and advective processes; rather, it shows that high-energy particles enter the heliosphere, lose energy, and are swept out by the SW at lower energies.

The fluxes from the FTE depend on pitch angle, and one could, in theory, average them over pitch cosine (denoted by angular brackets in what follows, i.e. $\langle\cdots\rangle_\mu = \int_{-1}^{1}\cdots\,\mathrm{d}\mu/2$) and compare them with Eq. 50. However, the distribution function is unfortunately too noisy to allow this. Nonetheless, it remains insightful to consider the spatial fluxes of the FTE, namely,

$$J_r(\mu) = (\mu v b_r + u_r)\,f(\mu) - \mathsf{D}^\perp_{rr}(\mu)\,\frac{\partial f(\mu)}{\partial r}, \tag{53a}$$

$$J_\theta(\mu) = -\frac{\mathsf{D}^\perp_{\theta\theta}(\mu)}{r}\,\frac{\partial f(\mu)}{\partial\theta}, \tag{53b}$$

where $b_r = \cos\psi$ is the radial component of the unit Parker HMF vector (see Eq. A.2), $\mathsf{D}^\perp_{rr}(\mu) = h(\mu)\,\kappa_{\perp r}\sin^2\psi$ is the radial DC, and $\mathsf{D}^\perp_{\theta\theta}(\mu) = h(\mu)\,\kappa_{\perp\theta}$ is the polar DC (see Sect. 3.2.2; we again did not consider longitudinal flux because the model is longitude-independent). Note that the diffusive flux is due solely to perpendicular diffusion, whereas the radial advective flux now includes the streaming of GCRs along the field. For simplicity, the distribution can be expressed in terms of Legendre polynomials (see e.g. Beeck & Wibberenz 1986; Zank 2014). As an illustrative example, we examined only the first three polynomials, i.e.

$$f(\mu) \approx \left(1 + A_1\mu + A_2\frac{3\mu^2-1}{2}\right)F_0. \tag{54}$$

Although the second-order term is expected to be insignificant in the current scenario, the first- and second-order terms serve as examples of how one could anticipate odd and even terms to contribute in the following discussion. The pitch-angle averaged flux will then be

$$\langle J_r(\mu)\rangle_\mu \approx \left(\frac{v}{3}A_1 b_r + u_r - \frac{2}{5}\frac{\partial A_2}{\partial r}\kappa^\perp_{rr}\right)F_0 - \kappa^\perp_{rr}\left(1 + \frac{2}{5}A_2\right)\frac{\partial F_0}{\partial r}, \tag{55a}$$

$$\langle J_\theta(\mu)\rangle_\mu \approx -\frac{\kappa_{\theta\theta}}{r}\left[\frac{2}{5}\frac{\partial A_2}{\partial\theta}F_0 + \left(1 + \frac{2}{5}A_2\right)\frac{\partial F_0}{\partial\theta}\right], \tag{55b}$$

where we assumed that $h(\mu) = 3\mu^2$ and $\kappa^\perp_{rr} = \kappa_\perp\sin^2\psi$ is the perpendicular part of the radial isotropic DC.

This has an interesting consequence if the distribution is perfectly isotropic (i.e. if $f(\mu) = F_0$ or $A_1 = A_2 = 0$): the SW advection and perpendicular diffusion are the same as in the Parker TPE (see Eq. 50), but there is no parallel diffusion. This is expected because the Parker TPE is derived by perturbing the isotropic distribution and solving for the perturbed anisotropic component, which yields parallel diffusion (as discussed in Sect. 2). Therefore, a small degree of anisotropy is necessary to describe parallel diffusion. Including the first-order anisotropy, the non-zero inward streaming flux ($A_1 v F_0\cos\psi$ with $A_1 < 0$) accounts for pitch-angle scattering and other pitch-angle changes, but in the advective component of the flux rather than as parallel diffusion in the diffusive component. This follows from the fact that, to lowest order, anisotropy arises from a local balance among pitch-angle scattering, focusing, and the momentum and spatial gradients of F_0, which act as source terms (as noted in Sect. 2). Therefore, this flux would be larger over the poles, due to the less-wound HMF and larger parallel MFPs, which enable particle streaming, and at low energies in the inner heliosphere, because the spatial gradients of F_0 are larger under these circumstances. Although the pitch-angle-averaged fluxes from the FTE could thus differ quantitatively from those of the Parker TPE, they should be qualitatively similar, with only the interpretation of the fluxes differing. The qualitative difference between $A_1 v F_0\cos\psi$ and $-\kappa_\parallel\cos^2\psi(\partial F_0/\partial r)$ likely accounts for part of the disparity between the Parker and focused TPEs, but quantifying this difference remains challenging because of noise in the first-order anisotropy. Including the second-order anisotropy shows that the perpendicular diffusive flux differs from that expected from the Parker TPE. At the same time, additional advective fluxes might also arise from the spatial gradient of the second-order anisotropy. These modifications, however, are expected to be negligible due to the smallness of the second-order anisotropy. The anisotropy would also modify the momentum changes in Eq. 2b to

$$\left\langle\frac{\mathrm{d}p}{\mathrm{d}t}\right\rangle_\mu \approx -p\left\{\frac{A_2}{5}\hat{\boldsymbol{b}}\hat{\boldsymbol{b}}:\boldsymbol{\nabla}\boldsymbol{u} + \frac{1-A_2/5}{3}\boldsymbol{\nabla}\cdot\boldsymbol{u} + \frac{A_1}{3v}\hat{\boldsymbol{b}}\cdot\left[\frac{\partial\boldsymbol{u}}{\partial t} + (\boldsymbol{u}\cdot\boldsymbol{\nabla})\,\boldsymbol{u}\right]\right\}. \tag{56}$$

Although the contribution of the second-order anisotropy is minor for the GCRs considered here, the last term leads to slightly reduced energy losses (since $A_1\hat{\boldsymbol{b}}\cdot[(\boldsymbol{u}\cdot\boldsymbol{\nabla})\boldsymbol{u}] < 0$). However, it is apparent from Eq. A.7e that this term is significant only near the Sun in the equatorial regions, and therefore, this correction is likely negligible. These anisotropy-modified fluxes (note that the momentum flux is $(\mathrm{d}p/\mathrm{d}t)\,f(\mu)$ or $\langle\mathrm{d}p/\mathrm{d}t\rangle_\mu F_0$) highlight the additional terms required in the Parker TPE when the interplay between pitch-angle scattering and various physical processes is taken into account (as mentioned in Sect. 2).

In conclusion, the non-zero fluxes, particle streaming, and the increased importance of focusing over the poles imply an anisotropic distribution, as shown by the anisotropy proxy (bottom panel of Fig. 3). The Parker TPE does not model this anisotropy accurately, as indicated by the percentage deviation (top panel of Fig. 3). Physically, particles tend to stream along the HMF over the poles, where they experience less pitch-angle scattering and more focusing, perpendicular diffusion slowly transports them to the equator, and the SW advects them outward in the equatorial regions after they lose much of their energy. It appears more likely that GCRs diffuse from the poles towards the equator in the inner heliosphere than directly into the heliosphere in the equatorial region, because GCRs can more easily reach the inner heliosphere over the poles, owing to larger parallel MFPs compared with the smaller perpendicular MFPs in the equatorial regions (only the gradient of the small second-order anisotropy can oppose the polar diffusive flux from the poles to the equator, as per Eq. 55b). The streaming of GCRs over the poles and the focusing they undergo there are unavoidable consequences of the HMF geometry used here and of the typical assumptions about DCs over the poles, which lead to large parallel MFPs. Although focusing might be expected to play a lesser role in the outer heliosphere than near the Sun, the large parallel MFPs over the poles imply that pitch-angle scattering is ineffective at isotropising the distribution if any other process causes anisotropy. One might wonder how this scenario over the poles differs from the so-called 'scatter-free events' of SEPs (referring to events with very large parallel MFPs or to field-aligned particles arriving first at an observer). Perhaps the two scenarios are similar, but we advise against using that term because we believe there is no such thing as a 'scatter-free event'. Turbulence is omnipresent in the heliosphere and continually subjects all charged particles to small-scale pitch-angle scattering, even though the parallel MFP might be large (see the discussions by van den Berg et al. 2020; van den Berg 2023). What remains true is that particles stream more efficiently along the magnetic field when pitch-angle scattering is weak. The resulting anisotropy is very small compared with that observed during SEP events, yet the disproportionately large deviation between the Parker and focused TPEs is not due to the Parker TPE incorrectly modelling a small anisotropy at a single point but stems from the systematic accumulation of this incorrect modelling across the entire heliosphere. This also accounts for the spatial mismatch between the anisotropy proxy and the difference between the Parker and focused TPEs shown in Fig. 3. One might naively expect streaming over the poles to be more efficient than parallel diffusion, implying that the FTE should produce a higher intensity than the Parker TPE. However, pitch-angle scattering disrupts streaming and causes parallel diffusion; if scattering is infrequent, the resulting parallel diffusion in the Parker TPE appears over-diffusive. If streaming with inefficient pitch-angle scattering is treated as effective parallel diffusion, the Parker TPE would overestimate the particle diffusion rate into the heliosphere, leading to less modulation than in the FTE.

The question arises whether including the modifying terms that follow from deriving a diffusion-advection equation from the FTE could reduce the difference between the results of the Parker and the focused TPEs. Given that the omnidirectional intensity and first-order anisotropy resulting from the FTE were not statistically sensitive to the assumed pitch-angle dependencies of the DCs, we can consider the simplest case of isotropic pitch-angle scattering with pitch-angle-independent perpendicular diffusion in the current discussion. In this case, the modifying terms given by van den Berg (2023) simplify considerably, and the remaining terms arise from the interplay of pitch-angle scattering, focusing, and pitch-angle-dependent energy changes. Focusing modifies the parallel DC (as expected from Beeck & Wibberenz 1986; He & Schlickeiser 2014; Wang & Qin 2018), while the derivation adds additional advection parallel to the magnetic field, momentum changes, mixed parallel and momentum diffusion, and momentum diffusion terms to the Parker TPE (as expected from Wang & Qin 2018). Although the modifying terms can be analytically derived for these likely oversimplified DCs, they remain cumbersome to work with, and the direction and magnitude of these terms remain unclear. Without evaluating the terms, we can only say that they are polynomials in $\lambda_{\|}/L^{'}$. It may well be that a modified Parker TPE could come closer to the FTE result, but one would need to calculate many complex transport coefficients for something that is still only an approximation of the FTE, as one cannot get past the fact that $\lambda_{\|} > |L^{'}|$ over the poles, in which case it seems easier just to solve the FTE. This new equation would most definitely not be the standard Parker equation used in numerous GCR modulation studies, and would therefore yield different results. Solving this more complex TPE is beyond the scope of the current investigation, which sought to determine whether the standard Parker TPE and FTE yield comparable results under typical GCR modulation conditions.

We have taken care in this work to make the Parker and focused TPEs as comparable as possible by normalising the pitch-angle-dependent DCs in the FTE to the isotropic DCs of the Parker TPE. However, the current model lacks two key components that warrant further investigation. Firstly, future work should employ realistic scattering theories to calculate the DCs and use inputs from turbulence transport modelling. Given, however, the large MFPs in the polar regions and the outer heliosphere predicted by most scattering theories for realistic turbulence parameters (see e.g. the comparison in Engelbrecht et al. 2022a), it is reasonable to expect the discrepancy between the Parker and focused TPEs to become even more pronounced in this case. Secondly, we did not include particle drifts here, as we had already identified a difference between the Parker and focused TPEs when diffusion alone was considered. To realistically include drifts, one should first address the questions of pitch-angle-dependent neutral sheet drift and turbulent drift reduction[7]. Nevertheless, we can speculate that the difference between the Parker and focused TPEs would be greater for $qA > 0$, where q is the particle charge and A is the polarity of the Sun's north pole. This is because positively charged GCRs drift in from the poles and out along the heliospheric current sheet when $qA > 0$, thereby adding to the flux patterns reported here. Although the drift pattern is reversed for $qA < 0$, it might not reduce the reported flux patterns, because CRs still experience large MFPs in the outer heliosphere and over the poles. Additionally, incorporating pitch-angle-dependent diffusive shock acceleration at the termination shock (see e.g. le Roux et al. 2007) or non-axisymmetric, pitch-angle-dependent diffusion across the heliopause (see e.g. Strauss & Fichtner 2014; Strauss et al. 2016) could produce other interesting differences between the solutions of the Parker and focused TPEs. The latter case could be more intricate if the very-local interstellar spectrum

[7] van den Berg et al. (2021) present an initial theoretical and modelling investigation; however, further work is necessary to verify and refine it.

is also anisotropic, as is evident from Voyager 1 observations of GCR proton anisotropies after crossing the heliopause (see Rankin et al. 2019). Finally, the differences between the Parker and focused TPE reported by van den Berg (2023), arising from the interplay between pitch-angle scattering and pitch-angle-dependent perpendicular diffusion when $\kappa_\perp \sim \kappa_\parallel$, might be evident in any astrophysical scenario with isotropic turbulence. Unfortunately, one cannot quantify the impact of modulation in the heliosheath, at the termination shock, due to drifts, or of using more realistic MFPs on the difference between the Parker and focused TPEs without further numerical modelling.

6. Summary and conclusion

In this work, we used transport coefficients and heliospheric model parameters commonly employed in GCR modulation studies, which solve the Parker TPE under solar-minimum conditions and accurately reproduce GCR intensity observations at Earth's orbit. In this model, the Parker TPE yields results that differ from those obtained by solving the FTE under the same conditions. These differences vary with particle energy and position in the heliosphere, reaching $\sim$ 30% at lower kinetic energies when comparing intensities at Earth, and up to $\sim$ 40% over the poles at the same energy and radial distance. This difference is comparable to the year-to-year variation in observations caused by solar activity (see e.g. Vos 2011; Adriani et al. 2013; Potgieter et al. 2014; Raath 2015; Martucci et al. 2018). However, the specific difference may not be a fixed value and is likely influenced by the particular DCs and transport conditions used here. Nonetheless, this deviation arises from small first-order anisotropies that are particularly significant at lower energies in the polar regions between $\sim 20 - 40$ au. Limited observations of GCR anisotropies, typically at high energies $>$ 1 TeV (see e.g. Amenomori et al. 2006; Guillian et al. 2007; Bartoli et al. 2018; Abeysekara et al. 2019; Chakraborty et al. 2024; Maalal & Zhang 2025), suggest that the anisotropies are indeed small (see e.g. Adriani et al. 2015 and Ajello et al. 2019 for lower energies $<$ 1 GeV). Particle fluxes indicate that inward particle streaming along the HMF in the polar regions, a natural and unavoidable consequence of the Parker HMF model used here, produces the anisotropy patterns. The less-wound magnetic field lines in the polar regions, together with the larger parallel MFPs there, provide a natural highway for particles to stream into the inner heliosphere. The anisotropy pattern does not match the spatial pattern of the difference between the two TPEs. This is most likely not due to the Parker TPE incorrectly modelling the small anisotropy at a single point, but rather to the cumulative effect of incorrect modelling across the entire heliosphere (particularly affecting low-energy particles, which spend more time being modulated). Additionally, streaming of particles coupled with weak pitch-angle scattering cannot be accurately described as effective parallel diffusion (see the discussion in van den Berg 2023), leading to the Parker TPE becoming over-diffusive (this may partly explain why diffusive transport sometimes fails to account for certain observations; see Effenberger et al. 2025 for a review). Furthermore, the FTE yields nearly identical results across different pitch-angle dependencies of the DCs. This suggests that spectral and anisotropy data from GCR observations alone cannot distinguish among various scattering theories for the pitch-angle dependence of DCs that yield similar MFPs. This highlights the importance of testing scattering theories against full-orbit simulation results (see e.g. Els et al. 2024; van den Berg et al. 2024) before applying them in TPEs and reinforces the argument that both numerical and observational studies of the PAD are necessary.

Given the significant difference in GCR intensities at Earth computed using the Parker TPE versus the FTE, one may question whether precision studies of GCR modulation, where precision means highly accurate fits of model results to detailed observations, are truly meaningful. One can certainly choose DCs to match the Parker TPE to observations. However, this work indicates that FTE results are no longer comparable with observations when using the same effective MFPs. Therefore, the spatial and energy dependencies, as well as the magnitudes of these effective DCs inferred from the Parker TPE, might not be comparable to even the best theoretical predictions for the DCs. Conversely, fitting observations with the FTE may yield MFPs larger than those inferred from fitting the Parker TPE. One should take this into account when discussing and applying the Palmer (1982) consensus values (see also Bieber et al. 1994; Engelbrecht et al. 2022b). Given these findings, it becomes even less clear when lower-dimensional approximate solutions to the Parker TPE, such as the commonly used force-field approximation (see e.g. Gleeson & Axford 1968; Quenby 1984; Moraal 2013), can provide meaningful insights into the physics behind GCR modulation, given their well-defined limitations as solutions to the Parker TPE (see e.g. Caballero-Lopez & Moraal 2004; Engelbrecht & Di Felice 2020). Nonetheless, for qualitative studies of GCR modulation, the Parker TPE, which describes the broader physical processes governing particle transport, is expected to yield reliable qualitative results. This, however, is subject to a caveat, particularly when the Parker TPE is applied in exotic scenarios, such as different astrospheres, where transport conditions can vary significantly from those in the heliosphere. This is particularly true for the astrospheres of slowly rotating stars, where the less-wound magnetic field leads to a greater contribution from parallel diffusion to the radial DC (see e.g. Mesquita et al. 2021; Engelbrecht et al. 2024), thereby exacerbating the discrepancies discussed here. However, the larger uncertainties inherent in such endeavours (see e.g. Herbst et al. 2022) may outweigh those arising from using the Parker TPE.

The FTE describes transport processes in more detail than the Parker TPE. Some of the crudest approximations in the Parker TPE involve assuming that $d\mu/dt = 0$ and neglecting the interplay between pitch-angle scattering and other pitch-angle-dependent processes. Of course, one could try to improve agreement between the TPEs by including as many modifying terms as possible in the Parker TPE to account for interplay among processes or by using a higher-order approximation of the FTE, such as a telegraph equation. However, such a TPE would still remain only a more refined approximation of the FTE. These additional DCs also imply that any parallel (perpendicular) DC inferred from fitting the Parker TPE to observations is an 'effective parallel (or perpendicular) DC' that includes diffusion contributions from all physical processes, not just from pitch-angle scattering (cross-field diffusion). For precise modelling in the heliosphere, eliminating the uncertainties inherent in the differences between the Parker and focused TPEs requires solving the full FTE. Although solving the FTE is computationally more challenging than solving the Parker TPE, the hope is that the CR modelling community will embrace the opportunity to deepen their understanding of CR modulation through transport modelling at the pitch-angle level. The community may need to revisit earlier conclusions about the global modulation of GCRs in the heliosphere. In particular, future work should explore the effects of the processes discussed in the last paragraph of Sect. 5, which the current study does not include, and quantify their influence on the differences between the Parker and focused TPE results.

Acknowledgements. JPvdB acknowledges partial support from the South African National Space Agency for the initial theoretical work. JPvdB also thanks J. Light for discussions about finite-difference methods. This research was supported by the International Space Science Institute (ISSI) in Bern through the ISSI International Team project No. 24-608 ("Energetic Particle Transport in Space Plasma Turbulence"). The authors thank the anonymous reviewer for their comments. The C code used the permuted congruential generator (O'Neill 2014) and Open MPI (Gabriel et al. 2004). Figures were prepared with Matplotlib (Hunter 2007), and certain calculations were performed with NumPy (Harris et al. 2020) and SciPy (Virtanen et al. 2020). Claude (Sonnet 4.6; free plan) was used to organise parts of the manuscript and identify where explanations are required, while Claude (Sonnet 4.6; pro plan) was also used to identify where the manuscript did not adhere to the journal's language guidelines. Grammarly (pro plan) was used to improve the language of the manuscript.

References

Abeysekara, A. U., Alfaro, R., Alvarez, C., et al. 2019, ApJ, 871, 96
Adriani, O., Barbarino, G. C., Bazilevskaya, G. A., et al. 2013, ApJ, 765, 91
Adriani, O., Barbarino, G. C., Bazilevskaya, G. A., et al. 2015, ApJ, 811, 21
Agueda, N. & Vainio, R. 2013, J. Space Weather Space Clim., 3, A10
Agueda, N., Vainio, R., Lario, D., & Sanahuja, B. 2008, ApJ, 675, 1601
Ajello, M., Baldini, L., Barbiellini, G., et al. 2019, ApJ, 883, 33
Amenomori, M., Ayabe, S., Bi, X. J., et al. 2006, Sci., 314, 439
Bartoli, B., Bernardini, P., Bi, X. J., et al. 2018, ApJ, 861, 93
Beeck, J. & Wibberenz, G. 1986, ApJ, 311, 437
Bieber, J., Matthaeus, W. H., Smith, C. W., et al. 1994, ApJ, 420, 294
Breech, B., Matthaeus, W. H., Minnie, J., et al. 2005, Geophys. Res. Lett., 32, L06103
Burger, R. A., Krüger, T. P. J., Hitge, M., & Engelbrecht, N. E. 2008, ApJ, 674, 511
Burger, R. A., Moraal, H., & Webb, G. M. 1985, Ap&SS, 116, 107
Burger, R. A., Potgieter, M. S., & Heber, B. 2000, J. Geophys. Res., 105, 27447
Caballero-Lopez, R. A. & Moraal, H. 2004, J. Geophys. Res.(Space Phys.), 109, A01101
Chakraborty, M., Ahmad, S., Chandra, A., et al. 2024, ApJ, 961, 87
Chenette, D. L., Conlon, T. F., Pyle, K. R., & Simpson, J. A. 1977, ApJ, 215, L95
Dunzlaff, P., Kopp, A., & Heber, B. 2010, J. Geophys. Res.(Space Phys.), 115, A10106
Effenberger, F. & Litvinenko, Y. E. 2014, ApJ, 783, 15
Effenberger, F., Walter, D., Fichtner, H., et al. 2025, Space Sci. Rev., 221, 75
Els, P. L., Engelbrecht, N. E., Lang, J. T., & Strauss, R. D. 2024, ApJ, 975, 134
Engelbrecht, N. E. 2017, ApJ, 849, L15
Engelbrecht, N. E. 2019, ApJ, 880, 60
Engelbrecht, N. E. 2024, ApJ, 975, 227
Engelbrecht, N. E. & Burger, R. A. 2013a, ApJ, 772, 46
Engelbrecht, N. E. & Burger, R. A. 2013b, ApJ, 779, 158
Engelbrecht, N. E. & Di Felice, V. 2020, Phys. Rev. D, 102, 103007
Engelbrecht, N. E., Effenberger, F., Florinski, V., et al. 2022a, Space Sci. Rev., 218, 33
Engelbrecht, N. E., Herbst, K., Strauss, R. D. T., et al. 2024, ApJ, 964, 89
Engelbrecht, N. E., Vogt, A., Herbst, K., Strauss, R. D. T., & Burger, R. A. 2022b, ApJ, 929, 8
Ferreira, S. E. S., Potgieter, M. S., Burger, R. A., Heber, B., & Fichtner, H. 2001, J. Geophys. Res., 106, 24979
Gabriel, E., Fagg, G. E., Bosilca, G., et al. 2004, in Proc. 11th European PVM/MPI Users' Group Meeting, Budapest, Hungary, 97
Gardiner, C. W. 1994, Handbook of stochastic methods for physics, chemistry and the natural sciences (Springer-Verlag)
Giacalone, J. & Jokipii, J. R. 1999, ApJ, 520, 204
Gleeson, L. J. & Axford, W. I. 1968, ApJ, 154, 1011
Gleeson, L. J. & Urch, I. H. 1971, Ap&SS, 11, 288
Gradshteyn, I. S. & Ryzhik, I. M. 2007, Table of integrals, series, and products, 7th edn., ed. A. Jeffrey & D. Zwillinger (Academic Press)
Guillian, G., Hosaka, J., Ishihara, K., et al. 2007, Phys. Rev. D, 75, 062003
Harris, C. R., Millman, K. J., van der Walt, S. J., et al. 2020, Nature, 585, 357
Hasselmann, K. & Wibberenz, G. 1970, ApJ, 162, 1049
He, H.-Q. & Schlickeiser, R. 2014, ApJ, 792, 85
Herbst, K., Baalmann, L. R., Bykov, A., et al. 2022, Space Sci. Rev., 218, 29
Hunter, J. D. 2007, Computing Sci. Eng., 9, 90
Isenberg, P. A. 1997, J. Geophys. Res., 102, 4719
Isenberg, P. A. & Jokipii, J. R. 1979, ApJ, 234, 746
Jokipii, J. R. & Parker, E. N. 1970, ApJ, 160, 735
Kloeden, P. E. & Platen, E. 1995, Numerical solution of stochastic differential equations, 2nd edn. (Springer-Verlag)
Kopp, A., Büsching, I., Strauss, R. D., & Potgieter, M. S. 2012, Comp. Phys. Comm., 183, 530
Kóta, J. 2013, Space Sci. Rev., 176, 391
Lampa, F. 2011, PhD thesis, University of Osnabrück, Germany
Lang, J. T., Strauss, R. D., Engelbrecht, N. E., et al. 2024, ApJ, 971, 105
le Roux, J. A. & Webb, G. M. 2012, ApJ, 746, 104
le Roux, J. A., Webb, G. M., Florinski, V., & Zank, G. P. 2007, ApJ, 662, 350
le Roux, J. A., Webb, G. M., & Ye, J. 2014, in Astro. Society Pacific Conf. Series, Vol. 484, Outstanding problems in heliophysics: From coronal heating to the edge of the heliosphere, ed. Q. Hu & G. P. Zank, 110
Litvinenko, Y. E. & Noble, P. L. 2013, ApJ, 765, 31
Litvinenko, Y. E. & Schlickeiser, R. 2013, A&A, 554, A59
Maalal, N. D. & Zhang, M. 2025, ApJ, 992, 46
Malkov, M. A. 2017, Phys. Rev. D, 95, 023007
Malkov, M. A. 2018, Nuc. Part. Phys. Proc., 297-299, 152
Martucci, M., Munini, R., Boezio, M., et al. 2018, ApJ, 854, L2
Matthaeus, W. H., Qin, G., Bieber, J. W., & Zank, G. P. 2003, ApJ, 590, L53
McComas, D. J., Barraclough, B. L., Funsten, H. O., et al. 2000, J. Geophys. Res., 105, 10419
McKibben, R. B., Zhang, M., Heber, B., Kunow, H., & Sanderson, T. R. 2007, Planet. Space Sci., 55, 21
Mesquita, A. L., Rodgers-Lee, D., & Vidotto, A. A. 2021, MNRAS, 505, 1817
Minnie, J., Bieber, J. W., Matthaeus, W. H., & Burger, R. A. 2007, ApJ, 670, 1149
Moloto, K. D., Engelbrecht, N. E., & Burger, R. A. 2018, ApJ, 859, 107
Moraal, H. 2013, Space Sci. Rev., 176, 299
Moses, D. 1987, ApJ, 313, 471
O'Neill, M. E. 2014, PCG: A family of simple fast space-efficient statistically good algorithms for random number generation, Tech. Rep. HMC-CS-2014-0905, Harvey Mudd College, Claremont, CA
Owens, M. J. & Forsyth, R. J. 2013, Living Rev. Solar Phys., 10, 5
Palmer, I. D. 1982, Rev. Geophys. Space Phys., 20, 335
Parker, E. N. 1958, ApJ, 128, 664
Parker, E. N. 1965, Planet. Space Sci., 13, 9
Parker, E. N. 1967, Planet. Space Sci., 15, 1723
Pei, C., Bieber, J. W., Burger, R. A., & Clem, J. 2010, J. Geophys. Res.(Space Phys.), 115, A12107
Potgieter, M. S. 2013, Living Rev. Solar Phys., 10, 3
Potgieter, M. S., Vos, E. E., Boezio, M., et al. 2014, Sol. Phys., 289, 391
Press, W. H., Teukolsky, S. A., Vetterling, W. T., & Flannery, B. P. 1992, Numerical recipes in C: The art of scientific computing (Cambridge University Press)
Pyle, K. R. & Simpson, J. A. 1977, ApJ, 215, L89
Qin, G. 2007, ApJ, 656, 217
Qin, G. & Shalchi, A. 2014, Applied Phys. Res., 6, 1
Quenby, J. J. 1984, Space Sci. Rev., 37, 201
Raath, J. L. 2015, A comparative study of cosmic ray modulation models
Rankin, J. S., Bindi, V., Bykov, A. M., et al. 2022, Space Sci. Rev., 218, 42
Rankin, J. S., Stone, E. C., Cummings, A. C., et al. 2019, ApJ, 873, 46
Roelof, E. C. 1969, in Lec. High-Energy Astrophys., ed. H. Ögelman & J. R. Wayland, 111
Rossi, B. & Olbert, S. 1970, Introduction to the physics of space. (McGraw-Hill)
Ruffolo, D. 1995, ApJ, 442, 861
Ruffolo, D., Chuychai, P., & Matthaeus, W. H. 2006, ApJ, 644, 971
Ruffolo, D., Chuychai, P., Wongpan, P., et al. 2008, ApJ, 686, 1231
Schlickeiser, R. 2002, Cosmic ray astrophysics (Springer-Verlag)
Schlickeiser, R. 2011, ApJ, 732, 96
Shalchi, A. 2010, ApJ, 720, L127
Shalchi, A. 2020, Space Sci. Rev., 216, 23
Sheeley, N. R., Wang, Y.-M., Hawley, S. H., et al. 1997, ApJ, 484, 472
Skilling, J. 1971, ApJ, 170, 265
Smith, E. J., Tsurutani, B. T., Chenette, D. L., Conlon, T. F., & Simpson, J. A. 1976, J. Geophys. Res., 81, 65
Steenkamp, R. 1995, PhD thesis, Potchefstroom University for Christian Higher Education
Stone, E. C., Cummings, A. C., McDonald, F. B., et al. 2013, Sci., 341, 150
Strauss, R. D., Dresing, N., Engelbrecht, N. E., et al. 2024, ApJ, 961, 57
Strauss, R. D. & Fichtner, H. 2014, A&A, 572, L3
Strauss, R. D. & Fichtner, H. 2015, ApJ, 801, 29
Strauss, R. D., le Roux, J. A., Engelbrecht, N. E., Ruffolo, D., & Dunzlaff, P. 2016, ApJ, 825, 43
Strauss, R. D., Potgieter, M. S., & Ferreira, S. E. S. 2011, Adv. Space Res., 48, 65
Strauss, R. D., Potgieter, M. S., Ferreira, S. E. S., & Hill, M. E. 2010, A&A, 522, A35
Strauss, R. D., van den Berg, J. P., & Rankin, J. S. 2022, ApJ, 928, 22
Strauss, R. D. T. & Effenberger, F. 2017, Space Sci. Rev., 212, 151
van den Berg, J. P. 2023, PhD thesis, North-West University, South Africa

van den Berg, J. P., Els, P. L., & Engelbrecht, N. E. 2024, ApJ, 977, 174
van den Berg, J. P., Engelbrecht, N. E., Wijsen, N., & Strauss, R. D. 2021, ApJ, 922, 200
van den Berg, J. P., Strauss, R. D. T., & Effenberger, F. 2020, Space Sci. Rev., 216, 146
Virtanen, P., Gommers, R., Oliphant, T. E., et al. 2020, Nat. Meth., 17, 261
Vogt, A., Engelbrecht, N. E., Strauss, R. D., et al. 2020, A&A, 642, A170
Vos, E. E. 2011, Cosmic ray modulation processes in the heliosphere
Wang, J. F. & Qin, G. 2018, ApJ, 868, 139
Webb, G. M. & Gleeson, L. J. 1979, Ap&SS, 60, 335
Wijsen, N. 2020, PhD thesis, KU Leuven, Belgium & Universitat de Barcelona, Spain
Wolfram|Alpha. 2026, (accessed 25 March 2026) https://www.wolframalpha.com/
Zank, G. P. 2014, Transport processes in space physics and astrophysics, Vol. 877 (Springer)
Zhang, M. 2006, J. Geophys. Res.(Space Phys.), 111, A04208
Zhao, L.-L., Adhikari, L., Zank, G. P., Hu, Q., & Feng, X. S. 2017, ApJ, 849, 88

Appendix A: Mathematical details of the model

In Sect. 3.2, Eqs 30 and 36 still require several derivatives, which we provide here for completeness. The magnitude of the HMF is (Vos 2011; Raath 2015)

$$B = B_{\rm P}\left(\frac{r_\oplus}{r}\right)^2 \sec\psi, \tag{A.1}$$

and the unit vector along the magnetic field is (Vos 2011; Raath 2015; Strauss & Fichtner 2015)

$$\hat{\boldsymbol{b}} = \cos\psi\,\hat{\boldsymbol{r}} - \sin\psi\,\hat{\boldsymbol{\phi}}, \tag{A.2}$$

where

$$\cos\psi = \frac{1}{\sqrt{1+\tan^2\psi}} = \frac{1}{\sqrt{1+\omega_\odot^2(r-r_\odot)^2\sin^2\theta/v_{\rm sw}^2}}, \tag{A.3a}$$

$$\sin\psi = \frac{\tan\psi}{\sqrt{1+\tan^2\psi}} = \frac{\omega_\odot(r-r_\odot)\sin\theta/v_{\rm sw}}{\sqrt{1+\omega_\odot^2(r-r_\odot)^2\sin^2\theta/v_{\rm sw}^2}}, \tag{A.3b}$$

and one should remember that $v_{\rm sw}(r,\theta)$.

Using

$$\frac{\partial}{\partial r}[\cos\psi] = -\left(\frac{1}{r-r_\odot} - \frac{1}{v_{\rm sw}}\frac{\partial v_{\rm sw}}{\partial r}\right)\sin^2\psi\cos\psi, \tag{A.4a}$$

$$\frac{\partial}{\partial\theta}[\cos\psi] = -\left(\cot\theta - \frac{1}{v_{\rm sw}}\frac{\partial v_{\rm sw}}{\partial\theta}\right)\sin^2\psi\cos\psi, \tag{A.4b}$$

$$\frac{\partial}{\partial r}[\sin\psi] = \left(\frac{1}{r-r_\odot} - \frac{1}{v_{\rm sw}}\frac{\partial v_{\rm sw}}{\partial r}\right)\sin\psi\cos^2\psi, \tag{A.4c}$$

$$\frac{\partial}{\partial\theta}[\sin\psi] = \left(\cot\theta - \frac{1}{v_{\rm sw}}\frac{\partial v_{\rm sw}}{\partial\theta}\right)\sin\psi\cos^2\psi, \tag{A.4d}$$

it can be calculated that

$$\frac{\partial b_r}{\partial r} = \left(\frac{1}{v_{\rm sw}}\frac{\partial v_{\rm sw}}{\partial r} - \frac{1}{r-r_\odot}\right)\sin^2\psi\cos\psi, \tag{A.5a}$$

$$\frac{\partial b_r}{\partial\theta} = \left(\frac{1}{v_{\rm sw}}\frac{\partial v_{\rm sw}}{\partial\theta} - \cot\theta\right)\sin^2\psi\cos\psi, \tag{A.5b}$$

$$\frac{\partial b_\phi}{\partial r} = \left(\frac{1}{v_{\rm sw}}\frac{\partial v_{\rm sw}}{\partial r} - \frac{1}{r-r_\odot}\right)\sin\psi\cos^2\psi, \tag{A.5c}$$

$$\frac{\partial b_\phi}{\partial\theta} = \left(\frac{1}{v_{\rm sw}}\frac{\partial v_{\rm sw}}{\partial\theta} - \cot\theta\right)\sin\psi\cos^2\psi, \tag{A.5d}$$

and

$$\frac{\partial B}{\partial r} = B\left[\left(\frac{1}{r-r_\odot} - \frac{1}{v_{\rm sw}}\frac{\partial v_{\rm sw}}{\partial r}\right)\sin^2\psi - \frac{2}{r}\right], \tag{A.6a}$$

$$\frac{\partial B}{\partial\theta} = B\left(\cot\theta - \frac{1}{v_{\rm sw}}\frac{\partial v_{\rm sw}}{\partial\theta}\right)\sin^2\psi. \tag{A.6b}$$

The derivatives of the HMF magnitude are required for the DC derivatives (not shown here).

The various terms entering Eqs 2b and 2c are (see le Roux et al. 2007 for the radial parts of these quantities)

$$\begin{aligned}\nabla\cdot\hat{\boldsymbol{b}} &= \frac{1}{r^2}\frac{\partial}{\partial r}\left[r^2 b_r\right] + \frac{1}{r\sin\theta}\frac{\partial b_\phi}{\partial\phi}\\ &= \left[\frac{2}{r} - \left(\frac{1}{r-r_\odot} - \frac{1}{v_{\rm sw}}\frac{\partial v_{\rm sw}}{\partial r}\right)\sin^2\psi\right]\cos\psi, \end{aligned}\tag{A.7a}$$

$$\begin{aligned}\nabla\cdot\boldsymbol{u} &= \frac{1}{r^2}\frac{\partial}{\partial r}\left[r^2 u_r\right] + \frac{1}{r\sin\theta}\frac{\partial u_\phi}{\partial\phi}\\ &= \frac{2v_{\rm sw}}{r} + \frac{\partial v_{\rm sw}}{\partial r}, \end{aligned}\tag{A.7b}$$

$$\begin{aligned}\hat{\boldsymbol{b}}\hat{\boldsymbol{b}}:\nabla\boldsymbol{u} &= b_r\left(b_r\frac{\partial u_r}{\partial r} + \frac{b_\phi}{r\sin\theta}\frac{\partial u_r}{\partial\phi} - \frac{b_\phi u_\phi}{r}\right) +\\ &\quad b_\phi\left(b_r\frac{\partial u_\phi}{\partial r} + \frac{b_\phi}{r\sin\theta}\frac{\partial u_\phi}{\partial\phi} + \frac{b_\phi u_r}{r}\right)\\ &= v_{\rm sw}\left[\left(\frac{1}{v_{\rm sw}}\frac{\partial v_{\rm sw}}{\partial r} - \frac{\tan^2\psi}{r}\right)\cos^2\psi + \right.\\ &\quad\left.\left(\frac{1}{r} + \frac{1}{r-r_\odot}\right)\sin^2\psi\right], \end{aligned}\tag{A.7c}$$

$$\begin{aligned}\hat{\boldsymbol{b}}\cdot\frac{\partial\boldsymbol{u}}{\partial t} &= b_r\frac{\partial u_r}{\partial t} + b_\phi\frac{\partial u_\phi}{\partial t}\\ &= 0, \end{aligned}\tag{A.7d}$$

$$\begin{aligned}\hat{b}\cdot[(\boldsymbol{u}\cdot\nabla)\boldsymbol{u}] &= b_r\left(u_r\frac{\partial u_r}{\partial r} + \frac{u_\phi}{r\sin\theta}\frac{\partial u_r}{\partial\phi} - \frac{u_\phi^2}{r}\right) +\\ &\quad b_\phi\left(u_r\frac{\partial u_\phi}{\partial r} + \frac{u_\phi}{r\sin\theta}\frac{\partial u_\phi}{\partial\phi} + \frac{u_r u_\phi}{r}\right)\\ &= v_{\rm sw}^2\left[\left(\frac{1}{v_{\rm sw}}\frac{\partial v_{\rm sw}}{\partial r} - \frac{\tan^2\psi}{r}\right)\cos\psi + \right.\\ &\quad\left.\left(\frac{1}{r} + \frac{1}{r-r_\odot}\right)\sin\psi\tan\psi\right]. \end{aligned}\tag{A.7e}$$

The derivatives of the elements in the isotropic diffusion tensor (Eq. 29) are

$$\begin{aligned}\frac{\partial\kappa_{rr}}{\partial r} &= \frac{\partial\kappa_\parallel}{\partial r}\cos^2\psi + \frac{\partial\kappa_{\perp r}}{\partial r}\sin^2\psi +\\ &\quad 2\kappa_{r\phi}\left(\frac{1}{r-r_\odot} - \frac{1}{v_{\rm sw}}\frac{\partial v_{\rm sw}}{\partial r}\right)\sin\psi\cos\psi, \end{aligned}\tag{A.8a}$$

$$\begin{aligned}\frac{\partial\kappa_{r\phi}}{\partial r} &= \left(\frac{\partial\kappa_{\perp r}}{\partial r} - \frac{\partial\kappa_\parallel}{\partial r}\right)\sin\psi\cos\psi +\\ &\quad \kappa_{r\phi}\left(\frac{1}{r-r_\odot} - \frac{1}{v_{\rm sw}}\frac{\partial v_{\rm sw}}{\partial r}\right)\left(\cos^2\psi - \sin^2\psi\right), \end{aligned}\tag{A.8b}$$

$$\frac{\partial\kappa_{\theta\theta}}{\partial\theta} = \frac{\partial\kappa_{\perp\theta}}{\partial\theta}, \tag{A.8c}$$

$$\frac{\partial\kappa_{\phi r}}{\partial\phi} = \left(\frac{\partial\kappa_{\perp r}}{\partial\phi} - \frac{\partial\kappa_\parallel}{\partial\phi}\right)\sin\psi\cos\psi, \tag{A.8d}$$

$$\frac{\partial\kappa_{\phi\phi}}{\partial\phi} = \frac{\partial\kappa_\parallel}{\partial\phi}\sin^2\psi + \frac{\partial\kappa_{\perp r}}{\partial\phi}\cos^2\psi. \tag{A.8e}$$

Similarly, for the perpendicular diffusion tensor (Eq. 35),

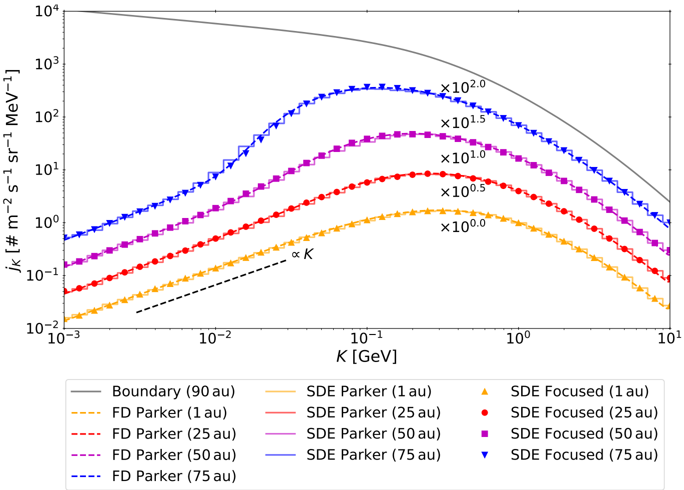

Fig. B.1: Comparison of spectra at different radial distances (different colours) as a function of kinetic energy between the SDE scheme of the 3D FTE (symbols), the SDE scheme of the 3D Parker TPE (steps), and an explicit FD scheme of the 1D Parker TPE (dashed lines). Spectra at various radial distances are multiplied by the indicated factor to make them clearly distinguishable.

$$\frac{\partial \mathrm{D}^{\perp}_{rr}}{\partial r} = \frac{\partial D_{\perp r}(\mu)}{\partial r} \sin^2\psi + 2\mathrm{D}^{\perp}_{rr}\left(\frac{1}{r - r_\odot} - \frac{1}{v_{\rm sw}}\frac{\partial v_{\rm sw}}{\partial r}\right)\cos^2\psi, \tag{A.9a}$$

$$\frac{\partial \mathrm{D}^{\perp}_{r\phi}}{\partial r} = \frac{\partial D_{\perp r}(\mu)}{\partial r} \sin\psi\cos\psi + \mathrm{D}^{\perp}_{r\phi}\left(\frac{1}{r - r_\odot} - \frac{1}{v_{\rm sw}}\frac{\partial v_{\rm sw}}{\partial r}\right)\left(\cos^2\psi - \sin^2\psi\right), \tag{A.9b}$$

$$\frac{\partial \mathrm{D}^{\perp}_{\theta\theta}}{\partial \theta} = \frac{\partial D_{\perp\theta}(\mu)}{\partial \theta}, \tag{A.9c}$$

$$\frac{\partial \mathrm{D}^{\perp}_{\phi r}}{\partial \phi} = \frac{\partial D_{\perp r}(\mu)}{\partial \phi} \sin\psi\cos\psi, \tag{A.9d}$$

$$\frac{\partial \mathrm{D}^{\perp}_{\phi\phi}}{\partial \phi} = \frac{\partial D_{\perp r}(\mu)}{\partial \phi} \cos^2\psi. \tag{A.9e}$$

The derivatives with respect to ϕ are all zero for the DCs in Sect. 3.1.

Appendix B: Model testing

We tested the SDE model presented in Sect. 3 by comparing its results with those from an explicit finite-difference (FD) model solving a 1D Parker TPE. We used a 1D model for simplicity, as incorporating more numerical dimensions into FD schemes is notoriously difficult. The model setup is the same as that presented in Caballero-Lopez & Moraal (2004), which is based on a model by Gleeson & Urch (1971). Therefore, consider a spherically symmetric heliosphere in which spatial variations depend only on the radial coordinate. Spherical symmetry would be fully achieved if the advection velocity and diffusion tensor are independent of latitude or longitude. This requires $\boldsymbol{V}_{\rm d} = \boldsymbol{0}$ and $\boldsymbol{v}_{\rm d}(\mu) = \boldsymbol{0}$, as already assumed, and $\kappa_\perp = \kappa_\parallel$, so that the diffusion tensor is diagonal in spherical coordinates. If there are no temporal dependencies, the system will relax into a stationary state. Expanding the spatial and momentum derivatives of the stationary ($\partial F_0/\partial t = 0$) version of Eq. 4 and keeping only the radial components, yields

$$-\frac{1}{3}\left(\frac{2u_r}{r} + \frac{\partial u_r}{\partial r}\right)\frac{\partial F_0}{\partial s} = \left(\frac{2\kappa_{rr}}{r} + \frac{\partial \kappa_{rr}}{\partial r} - u_r\right)\frac{\partial F_0}{\partial r} + \kappa_{rr}\frac{\partial^2 F_0}{\partial r^2}, \tag{B.1}$$

where $s = \ln p$. We utilised the SW speed and DC from Gleeson & Urch (1971) for this comparison, i.e.

$$u_r = V_{\rm sw}\left[1 - \mathrm{e}^{\eta(1 - r/r_\odot)}\right] \tag{B.2}$$

and

$$\kappa_{rr} = \kappa_0 \frac{v}{c}\left(\frac{r}{r_\oplus}\right)^{\alpha}\left(\frac{P}{P_{\rm r}}\right)^{\rho}, \tag{B.3}$$

respectively, where $\kappa_0 = 4.38 \times 10^{22}$ cm^2 s^{-1} = 0.7 au^2 h^{-1}, $\alpha = 0$ governs the radial dependence of the DC, and $\rho = 1$. For this comparison, we used the spectrum from Caballero-Lopez & Moraal (2004) at the outer boundary, i.e.

$$j_{\rm o}(K) = \frac{21.1\ \text{\# m}^{-2}\ \text{s}^{-1}\ \text{sr}^{-1}\ \text{MeV}^{-1}}{(K/K_{\rm r})^{2.8}\left[1 + 5.85(K_{\rm r}/K)^{1.22} + 1.18(K_{\rm r}/K)^{2.54}\right]}. \tag{B.4}$$

The details of various FD schemes are discussed by Gleeson & Urch (1971), Press et al. (1992), and Steenkamp (1995). In the FD scheme, we solved Eq. B.1 for $F_0(r, s)$ on an evenly spaced numerical grid, from the outer to the inner boundary (i.e. from $R_{\rm o}$ = 90 au to $r_\odot$ = 0.005 au, spaced by 0.2 au) and from the highest to the lowest energy (i.e. from 10 GeV to 1 MeV, spaced according to the CFL condition; see Press et al. 1992). This was done because $F_0(R_{\rm o}, s)$ is known (Eq. B.4) and we assumed that the spectrum remains unmodulated at sufficiently high energies, such that $F_0(r, 10\ \text{GeV}) = F_0(R_{\rm o}, 10\ \text{GeV})$ for all r. We first verified that the fully explicit, fully implicit, and Crank-Nicholson schemes all produced the same result (within 0.1%) under the CFL condition (not shown here). We then verified that the fully explicit scheme produced the same results as those reported by Caballero-Lopez & Moraal (2004) for different values of κ_0 and α (also not shown; Caballero-Lopez & Moraal 2004 showed how a similar spectrum can be obtained at Earth with different values of α if κ_0 is normalised to the same modulation parameter). We adapted the 3D SDE models to be compatible with the 1D FD model, as described above (i.e. by removing the latitudinal dependence of the SW and setting $\kappa_\perp = \kappa_\parallel$). Additionally, we computed the solution only at the equator, and we used isotropic pitch-angle scattering (Eq. 12a) with pitch-angle-independent perpendicular diffusion (Eq. 14 with $h = 1$) in the FTE. For the Parker and focused TPEs, we used 150 and 400 pseudo-particles per bin, respectively, with $\ell = 0.1$ for the adaptive time step (Eq. 24). The comparison between the fully explicit FD and SDE schemes is shown in Fig. B.1. Note, however, that more pseudo-particles are required, as we applied a three-point average over energy and radial position to the SDE results to smooth them. The agreement between the two SDE schemes and the FD scheme is excellent. Although this is expected for the FD and Parker-SDE schemes, both of which solve the Parker TPE, it is reassuring that the FTE yields the same result in this simplified setup. Figure B.1 also indicates the adiabatic limit of $j_K \propto K$

with a dashed black line at low energies. This demonstrates that the schemes accurately capture the physics of adiabatic energy losses, which dominate other processes at low energies (see e.g. Moraal 2013).

Appendix C: Pitch-angle distribution of anisotropic pitch-angle scattering

To calculate Eq. 46 for the PADC of Eq. 12b,

$$G(\mu) = \frac{v}{2L'}\int_{-1}^{\mu}\frac{1}{D_{\rm A}\left[|\eta|/(1+|\eta|)+\epsilon\right]}\,{\rm d}\eta = K_0\,\xi\int_{-1}^{\mu}\frac{1+|\eta|}{\epsilon+(1+\epsilon)\,|\eta|}\,{\rm d}\eta, \tag{C.1}$$

where $\xi = \lambda_{\|}/L^{'}$ and

$$K_n = \frac{2(1+\epsilon)^{4-n}}{3}\left[\frac{1}{6}+2\epsilon+\frac{5}{2}\epsilon^2+\frac{2}{3}\epsilon^3+ (1+2\epsilon)\ln\left(\frac{1+2\epsilon}{\epsilon}\right)\right]^{-1}, \tag{C.2}$$

one should consider the cases of negative and positive pitch cosine separately. When $\mu < 0$, the integral can be written as

$$\int_{-1}^{\mu}\frac{1-\eta}{\epsilon-(1+\epsilon)\,\eta}\,{\rm d}\eta = \frac{1}{1+\epsilon}\left[\eta-\frac{1}{1+\epsilon}\ln\left(\frac{\epsilon}{1+\epsilon}-\eta\right)-\frac{\ln(1+\epsilon)}{1+\epsilon}\right]_{-1}^{\mu} = \frac{1}{1+\epsilon}\left\{1+\mu+\frac{1}{1+\epsilon}\ln\left[\frac{1+2\epsilon}{\epsilon-(1+\epsilon)\,\mu}\right]\right\}, \tag{C.3}$$

while the integral can be written as

$$\int_{-1}^{0}\frac{1-\eta}{\epsilon-(1+\epsilon)\,\eta}\,{\rm d}\eta+\int_{0}^{\mu}\frac{1+\eta}{\epsilon+(1+\epsilon)\,\eta}\,{\rm d}\eta = \frac{1}{1+\epsilon}\left[1+\frac{1}{1+\epsilon}\ln\left(\frac{1+2\epsilon}{\epsilon}\right)\right]+ \frac{1}{1+\epsilon}\left[\eta+\frac{1}{1+\epsilon}\ln\left(\frac{\epsilon}{1+\epsilon}+\eta\right)+\frac{\ln(1+\epsilon)}{1+\epsilon}\right]_{0}^{\mu} = \frac{1}{1+\epsilon}\left\{1+\mu+\frac{1}{1+\epsilon}\ln\left[\frac{\epsilon+(1+\epsilon)\,\mu}{\epsilon^2/(1+2\epsilon)}\right]\right\} \tag{C.4}$$

when $\mu > 0$, where the previous expression was used to evaluate the first integral (see Eqs 2.111.1 and 2.111.5 of Gradshteyn & Ryzhik 2007 for the integrals). Hence, Eq. C.1 is a piecewise-continuous function, i.e.

$$G(\mu) = K_1\,\xi\left[1+\mu+\frac{1}{1+\epsilon}\left\{\begin{array}{ll}\ln\left[\frac{1+2\epsilon}{\epsilon-(1+\epsilon)\mu}\right] & \text{if} \quad \mu\le 0\\ \ln\left[\frac{\epsilon+(1+\epsilon)\mu}{\epsilon^2/(1+2\epsilon)}\right] & \text{if} \quad \mu > 0\end{array}\right.\right], \tag{C.5}$$

where $K_n = K_0\,(1+\epsilon)^{-n}$ was used.

Substituting this into Eq. 45, also yields a piecewise-continuous function for the PAD, i.e.

$$\tilde{f}_{\rm aniso}(\mu) = C\,{\rm e}^{K_1\,\xi\,\mu}\left\{\begin{array}{ll}\left[(1+\epsilon)\left(\frac{\epsilon}{1+\epsilon}-\mu\right)\right]^{-K_2\,\xi} & \text{if} \quad \mu\le 0\\ \left[\frac{1+\epsilon}{\epsilon^2}\left(\frac{\epsilon}{1+\epsilon}+\mu\right)\right]^{K_2\,\xi} & \text{if} \quad \mu > 0\end{array}\right., \tag{C.6}$$

where

$$C = (1+2\epsilon)^{K_2\,\xi}\,{\rm e}^{K_1\,\xi}\left[\int_{-1}^{1}{\rm e}^{G(\mu)}\,{\rm d}\mu\right]^{-1}. \tag{C.7}$$

Because the function is piecewise continuous, the normalisation integral can be split into negative and positive ranges, so that

$$\begin{aligned}&\int_{-1}^{1}{\rm e}^{G(\mu)}\,{\rm d}\mu\\ &= (1+2\epsilon)^{K_2\,\xi}\,{\rm e}^{K_1\,\xi}\left[(1+\epsilon)^{-K_2\,\xi}\int_{-1}^{0}{\rm e}^{K_1\,\xi\,\mu}\left(\frac{\epsilon}{1+\epsilon}-\mu\right)^{-K_2\,\xi}{\rm d}\mu + \left(\frac{1+\epsilon}{\epsilon^2}\right)^{K_2\,\xi}\int_{0}^{1}{\rm e}^{K_1\,\xi\,\mu}\left(\frac{\epsilon}{1+\epsilon}+\mu\right)^{K_2\,\xi}{\rm d}\mu\right]\\ &= \frac{(1+2\epsilon)^{K_2\,\xi}\,{\rm e}^{K_1\,\xi}}{K_1\,\xi}\,\Re\left\{(K_2\,\xi)^{K_2\,\xi}\,{\rm e}^{K_2\,\epsilon\,\xi}\left[\Gamma\left(1-K_2\,\xi, K_1\,\xi\left(\frac{\epsilon}{1+\epsilon}-\mu\right)\right)\right]_{-1}^{0} + \frac{{\rm e}^{-K_2\,\epsilon\,\xi}}{(-K_2\,\epsilon^2\,\xi)^{K_2\,\xi}}\left[\Gamma\left(1+K_2\,\xi, -K_1\,\xi\left(\frac{\epsilon}{1+\epsilon}+\mu\right)\right)\right]_{0}^{1}\right\}\\ &= \Re\,\frac{(1+2\epsilon)^{K_2\,\xi}\,(K_2\,\xi)^{K_2\,\xi}\,{\rm e}^{K_2\,(1+2\epsilon)\,\xi}}{K_1\,\xi}\left[\Gamma(1-K_2\,\xi, K_2\,\epsilon\,\xi)-\Gamma(1-K_2\,\xi, K_2\,(1+2\epsilon)\,\xi)\right] + \\ &\quad\Re\,\frac{(1+2\epsilon)^{K_2\,\xi}\,{\rm e}^{K_2\,\xi}}{K_1\,\xi\,(-K_2\,\epsilon^2\,\xi)^{K_2\,\xi}}\left[\Gamma(1+K_2\,\xi, -K_2\,(1+2\epsilon)\,\xi)-\Gamma(1+K_2\,\xi, -K_2\,\epsilon\,\xi)\right],\end{aligned} \tag{C.8}$$

where

$$\int_{x_1}^{x_2}{\rm e}^{ax}\,(c\pm x)^{\pm b}\,{\rm d}x = \Re\,\frac{(\mp 1)^{b}\,{\rm e}^{\mp ac}}{a^{1\pm b}}\,\Gamma\left(1\pm b, \mp a(c\pm x)\right)\Big|_{x_1}^{x_2} \tag{C.9}$$

was used for the integrals (calculated using Wolfram|Alpha 2026 with the prompts `integrate exp(a*x)*(c + x)^b` or `integrate exp(a*x)/(c - x)^b`), with $\Gamma(\alpha, z)$ the upper incomplete Gamma function.

Similarly, the first-order anisotropy (Eq. 41) can be calculated to be

$$\begin{aligned}A_1^{\rm aniso} &= 3\int_{-1}^{1}\mu\,\tilde{f}_{\rm aniso}(\mu)\,{\rm d}\mu\\ &= 3\,C\left[(1+\epsilon)^{-K_2\,\xi}\int_{-1}^{0}\mu\,{\rm e}^{K_1\,\xi\,\mu}\left(\frac{\epsilon}{1+\epsilon}-\mu\right)^{-K_2\,\xi}{\rm d}\mu + \left(\frac{1+\epsilon}{\epsilon^2}\right)^{K_2\,\xi}\int_{0}^{1}\mu\,{\rm e}^{K_1\,\xi\,\mu}\left(\frac{\epsilon}{1+\epsilon}+\mu\right)^{K_2\,\xi}{\rm d}\mu\right]\\ &= \frac{3\,C}{(K_1\,\xi)^2}\,\Re\left\{\left[K_2\,\epsilon\,\xi\,\Gamma\left(1-K_2\,\xi, K_1\,\xi\left(\frac{\epsilon}{1+\epsilon}-\mu\right)\right) - \Gamma\left(2-K_2\,\xi, K_1\,\xi\left(\frac{\epsilon}{1+\epsilon}-\mu\right)\right)\right]_{-1}^{0}(K_2\,\xi)^{K_2\,\xi}\,{\rm e}^{K_2\,\epsilon\,\xi} - \right.\\ &\quad\left.\left[K_2\,\epsilon\,\xi\,\Gamma\left(1+K_2\,\xi, -K_1\,\xi\left(\frac{\epsilon}{1+\epsilon}+\mu\right)\right) + \Gamma\left(2+K_2\,\xi, -K_1\,\xi\left(\frac{\epsilon}{1+\epsilon}+\mu\right)\right)\right]_{0}^{1}(-K_2\,\epsilon^2\,\xi)^{-K_2\,\xi}\,{\rm e}^{-K_2\,\epsilon\,\xi}\right\}\\ &= \Re\,\frac{3\,C\,(K_2\,\xi)^{K_2\,\xi}\,{\rm e}^{K_2\,\epsilon\,\xi}}{(K_1\,\xi)^2}\\ &\quad\{K_2\,\epsilon\,\xi\left[\Gamma(1-K_2\,\xi, K_2\,\epsilon\,\xi)-\Gamma(1-K_2\,\xi, K_2\,(1+2\epsilon)\,\xi)\right] - \left[\Gamma(2-K_2\,\xi, K_2\,\epsilon\,\xi)-\Gamma(2-K_2\,\xi, K_2\,(1+2\epsilon)\,\xi)\right]\} - \\ &\quad\Re\,\frac{3\,C}{(K_1\,\xi)^2(-K_2\,\epsilon^2\,\xi)^{K_2\,\xi}\,{\rm e}^{K_2\,\epsilon\,\xi}}\\ &\quad\{K_2\,\epsilon\,\xi\left[\Gamma(1+K_2\,\xi, -K_2\,(1+2\epsilon)\,\xi)-\Gamma(1+K_2\,\xi, -K_2\,\epsilon\,\xi)\right] + \Gamma(2+K_2\,\xi, -K_2\,(1+2\epsilon)\,\xi)-\Gamma(2+K_2\,\xi, -K_2\,\epsilon\,\xi)\},\end{aligned} \tag{C.10}$$

where

$$\int_{x_1}^{x_2} x\,\mathrm{e}^{ax}\,(c \pm x)^{\pm b}\,\mathrm{d}x = \Re\left[ac\,\Gamma\,(1 \pm b, \mp a(c \pm x)) \pm \Gamma\,(2 \pm b, \mp a(c \pm x))\right] \frac{(\mp 1)^{1-b}\,\mathrm{e}^{\mp ac}}{a^{2\pm b}}\Bigg|_{x_1}^{x_2} \tag{C.11}$$

was used for the integrals (calculated using Wolfram|Alpha 2026 with the prompts `integrate x*exp(a*x)*(c + x)^b` or `integrate (x*exp(a*x))/(c - x)^b`).